ARTICLE IN PRESS

Available online at www.sciencedirect.com

ScienceDirect

Advances in Space Research xxx (xxxx) xxx

ADVANCES IN SPACE RESEARCH (a COSPAR publication)

www.elsevier.com/locate/asr

Ring current electron precipitation during the 17 March 2013 geomagnetic storm: Underlying mechanisms and their effect on the atmosphere

Alina S. Grishina [a,b,*], Yuri Y. Shprits [a,b,c], Alexander Y. Drozdov [c], Miriam Sinnhuber [d], Florian Haenel [d], Dedong Wang [a], Mátyás Szabó-Roberts [a], Jan Maik Wissing [e], Stefan Bender [f]

[a] Department of Space Physics and Space Weather, GFZ German Research Centre for Geosciences, Albert-Einstein-Str 42-46, 14473 Potsdam, Germany
[b] Institute of Physics and Astronomy, University of Potsdam, Karl-Liebknecht-Str 24/25, 14476 Potsdam, Germany
[c] Department of Earth, Planetary and Space Sciences, University of California, Los Angeles, 595 Charles E Young Dr E, Los Angeles, CA 90095, USA
[d] Institute for Meteorology and Climate Research – Atmospheric Trace Gases and Remote Sensing (IMK-ASF), Karlsruhe Institute of Technology, Hermann-von-Helmholtz-Platz 1, 76344 Eggenstein-Leopoldshafen, Karlsruhe, Germany
[e] Institute for Solar-Terrestrial Physics, DLR German Aerospace Center Neustrelitz, Kalkhorstweg 53, 17235 Neustrelitz, Germany
[f] Instituto de Astrofísica de Andalucía, CSIC, Gta. de la Astronomía, s/n, 18008 Granada, Spain

Received 1 December 2023; received in revised form 4 March 2024; accepted 5 March 2024

Abstract

Electron and ion fluxes at energies of ~10 keV−1 MeV can change by orders of magnitude during geomagnetically active periods. This can lead to intensification of particle precipitation into the Earth's atmosphere. The process further affects atmospheric chemistry, which may impact weather and climate on the Earth's surface. In this study, we concentrate on ring current electrons, and investigate precipitation mechanisms using a numerical model based on the Fokker-Planck equation. We focus on a study of the main precipitation mechanisms, and their connection with atmospheric parameters. We investigate the 17 March 2013 storm using the convection–diffusion 4-Dimensional Versatile Electron Radiation Belt (VERB-4D) code, that allows us to quantify the impact of the storm on the electron ring current, and the resulting electron precipitation. We validate our results against observations from the Polar Operational Environmental Satellites (POES) mission, the low Earth orbiting meteorological satellites National Oceanic and Atmospheric Administration (NOAA-15,-16,-17,-18,-19), and Meteorological Operational Satellite MetOp-02, as well as the Van Allen Probes, and produce a data set of precipitating fluxes that covers an energy range from 10 keV to 1 MeV. We calculate the altitude-dependent atmospheric ionization rates, a prerequisite for atmospheric models to estimate effects of geomagnetically active periods on chemical and physical variability of the atmosphere at high latitudes. Atmospheric ionization rates are validated against Atmospheric Ionization during Substorm (AIMOS 2.1-Aisstorm) and Special Sensor Ultraviolet Spectrographic Imagers (SSUSI) values, and show good agreement at high geomagnetic latitudes during the storm time.

Keywords: Electron precipitation; Ring current; Ionization rates; Satellite observations; Geomagnetic storms

1. Introduction

The ring current is a region of enhanced particle flux in the Earth's magnetosphere consisting of energetic ions and

* Corresponding author.
E-mail address: alinag@gfz-potsdam.de (A.S. Grishina).

https://doi.org/10.1016/j.asr.2024.03.010
0273-1177/

electrons with energies ranging from several to hundreds of keV. While the ring current has been extensively studied over the past several decades, its role in influencing the Earth's upper atmosphere is still not fully understood. Electrons of energies from several to hundreds of keV precipitating into the atmosphere can have a significant impact on the chemical composition of the upper mesosphere and lower thermosphere, including the production of ozone depleting species like nitric oxides (NOx) (Barth, 2001; Sinnhuber et al., 2012, 2018). However, the quantitiative relationship of auroral versus ring current electrons in these changes is still not clear (Nesse Tyssøy et al., 2022; Sinnhuber and Funke, 2020; Sinnhuber et al., 2021).

Solar and magnetospheric events accompanied by large fluxes of precipitating protons or electrons can have a significant impact on the state of the atmosphere, initiated by the production of NOx in the mesosphere and lower thermosphere. NOx is transported down from the source regions into the stratosphere in large-scale downwelling motions during polar winter. It is called the "indirect effect" of energetic particle precipitation (Randall et al., 2007; Siskind et al., 2000; Solomon et al., 1982). Based on satellite observations, NOx produced by energetic particle precipitation (EPP) can be transported down into the middle stratosphere, as low as 25 km. EPP associated NOx contributes up to 40 % of total NOx at high latitudes during winter (Funke et al., 2014), and correlates with the geomagnetic activity indices (Funke et al., 2014; Sinnhuber et al., 2011). In the middle and upper stratosphere, nitric oxides significantly contribute to catalytic ozone loss. Simulations with and without EPP showed changes in ozone levels (Sinnhuber et al., 2018; Thorne, 1977; WMO, 2018), and EPP has been connected to a depletion of up to 60% of ozone at an altitude of 35–40 km (Randall et al., 2005; Sinnhuber et al., 2018). Such large changes in the radiatively active gas ozone affect the daily total radiative heating (Sinnhuber et al., 2018), initiating changes of dynamics throughout the atmosphere. Analyses of surface temperatures for periods of high and low geomagnetic activity or in different times of 11-year solar cycle suggest an impact even on tropospheric weather systems (Maliniemi et al., 2014; Seppälä et al., 2009), with morphologically similar changes to the atmospheric dynamics also predicted by atmospheric composition-climate models (Rozanov et al., 2005, 2012). Consequenly, EPP was recommended as a part of the solar forcing of the climate system for the Coupled Model Intercomparison Project (CMIP6) model experiments (Matthes et al., 2017); an improved set of recommendations is currently planned for the upcoming CMIP7 experiments (Funke et al., 2023).

In order to accurately model the precipitated flux, we need to understand the mechanism of precipitation. Wave-particle interactions is one of the most important mechanisms causing precipitation (Li et al., 2019). Magnetospheric waves play an important role in acceleration and scattering of particles. Whistler-mode chorus (Kasahara et al., 2018; Ma et al., 2020; Shprits et al., 2008b,a; Thorne, 2010; Wang and Shprits, 2019) and hiss (Li et al., 2019; Ma et al., 2021), electron cyclotron harmonic (ECH) waves (Teng et al., 2023; Zhang et al., 2015), kinetic Alfvén waves (Chaston et al., 2015; Ma et al., 2016; Malaspina et al., 2014) are the main drivers of electron precipitation at keV energies. Specifically, chorus waves affect precipitation in the energy range from 0.1 eV to multi-MeV. Chorus waves cause precipitation across a range of latitudes and radial distances (Thorne et al., 2005). The most significant electron precipitation due to chorus is found from the nightside to dawn sectors over radial distances from 4 to 6.5 according to Ni et al. (2014) and cause the most intensive precipitation in the dawn-to-noon sector according to Yu et al. (2022). Yakovchuk and Wissing (2019) show that night-time energetic electron precipitation is connected to substorm activity. The scattering of electrons with energies greater than 30 keV is a crucial consequence of the lower band chorus wave activity in that region (Lam et al., 2010). In particular, lower band chorus drives diffuse auroral precipitation (Yu et al., 2023). Hiss waves, unlike the chorus waves, are observed in the inner zone of the magnetosphere, restricted by the plasmapause. They are responsible for depletion of energetic (~10 keV–~1 MeV) electrons in the plasmasphere and plumes (Ma et al., 2015; Meredith et al., 2006; 2007; Summers et al., 2008) and for the formation of the slot region (Lyons and Thorne, 1973). Electromagnetic ion cyclotron (EMIC) waves affect scattering of multi-MeV electrons (Drozdov et al., 2020; Shprits et al., 2013).

Electron precipitation can be quantified by using the low-Earth orbit (LEO) satellites, e.g., SAMPEX (Tu et al., 2010), Lomonosov (Shprits et al., 2023), Focused Investigations of Relativistic Electron Bursts: Intensity, Range, and Dynamics (FIREBIRD II) CubeSats (Johnson et al., 2020) and ELFIN (Angelopoulos et al., 2020), as well as balloon measurements based on detection of bremsstrahlung X-rays (Bazilevskaya et al., 2020; Blum et al., 2013). Attempts to compare observed and simulated precipitated fluxes have also been made using observations from the LEO meteorological satellites Polar Operational Environmental Satellites (POES). Chen et al. (2019) used a self-consistent Rice Convection Model-Equilibrium (RCM-E) and parametrized wave-induced loss models following Orlova et al. (2014) and Orlova and Shprits (2014) to simulate both trapped electron fluxes in geostationary orbit (GEO) and precipitating fluxes in the ionosphere. They found that simulated precipitating electron energy flux is most intense from premidnight through the dawn side. Reidy et al. (2021) have calculated the precipitated flux using the diffusion coefficients provided by the British Antarctic Survey Radiation Belt Model (BAS-RBM, Glauert et al., 2014), and compared the results to POES measurements inside the loss cone for energies >30 keV and >100 keV. The authors found that the modeled and observed fluxes show good correlation on the dawn and dayside for $L^* > 5$, with magnitudes of the fluxes generally within a factor of 10 of each other during moderate

geomagnetic conditions. However, for magnetic local time (MLT) 18 − 24 h, $L^* = 6$ the ratio reaches values of $\sim 10^{-12}$ (see Fig. 9 in Reidy et al., 2021), which indicates underestimation of the modeling results in comparison to the observations. Ødegaard et al. (2017) applied a superposed epoch analysis of 41 CIR storms to estimate electron loss, using a combination of POES measurements and theory of pitch angle distribution from Kennel and Petschek (1966), to find a correlation between the solar wind parameters and enhanced precipitation. Van de Kamp et al. (2016) developed a geomagnetic index driven model for radiation belt electrons, based on the POES observations, and validated it against the Antarctic-Arctic Radiation-belt (Dynamic) Deposition-VLF Atmospheric Research Konsortium (AARDDVARK) network measurements. The model allows to calculate long-term ionization rate using Fang et al. (2010) parametrization. This model has been recommended for the CMIP6 experiment for medium-energy electrons (Matthes et al., 2017), as the only parametrized model that allows for extending the time series backward in time to 1850, which is necessary for climate reconstructions. The model predicts fluxes 1.7 times lower than those inferred from VLF signal analysis and POES observations (Clilverd et al., 2020). Nesse Tyssøy et al. (2019) also showed an underestimation of the modeled electron fluxes particularly during periods of high geomagnetic activity compared to fluxes observed by POES. Similarly, results from the van de Kamp/CMIP6 model showed the lowest ionization rates in an intercomparison between eight ionization rate data sets all based on POES electron fluxes during a geomagnetic storm in April 2010 (Nesse Tyssøy et al., 2022). Sanchez et al. (2022) showed high spatial localization of electron precipitation based on the Boulder Electron Radiation to Ionization (BERI) model, coupled with the diffusion model, and applied to Van Allen Probes.

In this study, we focus on the St. Patrick's Day geomagnetic storm. The storm emitted at the Sun as a coronal mass ejection that directed towards the Earth and traveled at a speed of 1400 km/s, which is relatively fast for such events (NASA, n.d.). In the past, coronal mass ejections at this speed resulted in mild to moderate effects on Earth, such as auroras near the poles. During the storm's onset on 17 March around 08:00 UT, there was an increase in radiation belt electron fluxes up to several orders of magnitude, based on the observations from the Van Allen Probes (e.g., Wang et al., 2020), at electron ring current energies of 50 keV and 200 keV within a radial distance of $L \sim 3$ to 5.8 (e.g., Shprits et al., 2015). These fluxes decreased during the recovery phase which began several hours later. However, during the main phase of the storm, the fluxes of 1 MeV electrons in the relativistic radiation belt showed a dropout at $L \sim 3.5$ to 5.8, and then gradually increased over several days during the recovery phase. The maximum Kp value, which is one of the indicators of geomagnetic activity, reached 6.7 during this period, and the minimum Dst index value was −132 nT, indicating strong geomagnetic activity.

There are multiple studies that attempted to model the St. Patrick's Day storm using diffusion processes. In the framework of the recent Geospace Environment Modeling (GEM) challenge, Wang et al. (2020) simulated radiation belt scenarios, and validated their results against Van Allen Probes, showing good reproducibility for this event. Another simulation with several hiss and chorus lifetime approximations was made by Ferradas et al. (2019). All three models of electron lifetimes showed good agreement during the storm main phase. The simulation with hiss losses by Orlova et al. (2016) and chorus losses by Orlova and Shprits (2014) yielded the most accurate match with the fluxes detected by the Van Allen Probes within the energy range of 20 eV to 100 keV. Wang et al. (2017) performed a simulation with A Layer Method with Monotonic Cubic interpolation (LM-MC), accounting for equatorial pitch angle (α_0), momentum (p), and L-shell coordinates. The flux enhancements and the energy-dependent pitch angle distribution profiles were reproduced in agreement with Van Allen Probes A and B observations. Using the Rice Convection Model-Equilibrium (RCM-E) model, Chen et al. (2019) reproduced the ring current electron, proton and ion fluxes in energy range ~37 to 150 keV. Additionally, precipitated fluxes were compared to Defence Meteorological Satellite Program (DMSP) observations and agreed well in predawn to mid-morning sectors.

Our work extends a previous study by Aseev et al. (2019), where they investigated the sensitivity of the ring current electron dynamics to the global electric field models, boundary conditions, electron lifetimes, radial diffusion and sub-auroral polarization streams (SAPS) using the 4-Dimensional Versatile Electron Radiation Belt (VERB-4D) code (Aseev et al., 2016; Shprits et al., 2015). The obtained discrepancy between the model and observations below 4.5 R_E could be explained by errors in the electron lifetimes model. For a better reproduction, the usage of other models accounting for the loss process is necessary. Authors used an empirical Denton et al. (2015) model for electron fluxes at the outer boundary, which showed a good agreement with observations from the Magnetospheric Plasma Analyzer (MPA) instrument on board Los Alamos National Laboratory (LANL) satellites 1994-084 during both quiet and disturbed conditions.

In this study, we use the ring current-radiation belt change throughout the VERB-4D code to accurately model the precipitating electron flux. From these electron fluxes, altitude-dependend profiles of atmospheric ionization rates are calculated using a commonly-used parameterization (Fang et al., 2010). These ionization rate profiles can be used as input data for atmospheric composition-climate models, and provide a new approach to constrain the effect of electrons with medium-range energy, in particular ring current and radiation belt electrons on the atmosphere. The paper is organized as follows: Section 2 describes the satellite data used for validation. Section 3 provides details on the model setup and tests. Section 4 shows our modeling

results. Section 5 discusses the implications of our results and possible reasons for the remaining inconsistency between the model output and observations. Section 6 concludes the paper.

2. Data

We use observations from four satellite missions in our study, both as our boundary condition in certain configuration, and as a way to validate our model output in the equatorial plane and closer to the Earth. The missions used are the Van Allen Probes, the Polar Operational Environmental Satellite (POES), Geostationary Operational Environmental Satellite (GOES), and Special Sensor Ultraviolet Spectrographic Imagers (SSUSI).

2.1. Van Allen Probes

The Van Allen Probes are a pair of twins of National Aeronautics and Space Administration (NASA) near-equatorial spacecraft. They were launched in 2012 to study the Earth's radiation belts. The satellites fly on an elliptical orbit with an average inclination of 10°, a perigee of 1.1 R_E, and apogee of 5.8 R_E. They are equipped with a suite of instruments that measure the energy and pitch angle resolved flux of the particles, as well as electromagnetic wave properties. The two particle instruments used in this study, the Helium Oxygen Proton Electron (HOPE) and Magnetic Electron Ion Spectrometer (MagEIS), measure the energy and direction of electrons, protons and ions in the radiation belts. HOPE measures electrons with energies from 1 eV to 50 keV (Funsten et al., 2013). MagEIS provides electron measurements over the range of energies 20 keV – 4 MeV (Blake, 2013; Spence et al., 2013). We used a combination of electron fluxes from both instruments for validation of the fluxes in the equatorial plane.

2.2. POES

POES is a series of polar-orbiting weather satellites operated by the United States' National Oceanic and Atmospheric Administration (NOAA). POES provides global coverage of atmospheric and surface conditions, which are used to support weather forecasting, environmental monitoring, and search and rescue operations. To validate our modeled precipitating fluxes against observations in the low Earth orbit, we use data provided by 6 meteorological POES satellites: NOAA-15, NOAA-16, NOAA-17, NOAA-18, NOAA-19 and Meteorological Operational Satellite MetOp-02. We use electron flux measurements from the Space Environment Monitor-2 Medium-Energy Proton and Electron Detector (SEM-2 MEPED) instrument, designed to measure flux and energy spectrum of medium energetic electrons and protons in two directions. The SEM-2 MEPED instrument consists of two sensors, one for electrons and one for protons, that cover an energy range from 30 keV to 2.6 MeV and from 30 keV to 6.9 MeV, respectively. These sensors are mounted on a boom that extends away from the satellite, to minimize the influence of spacecraft-generated particles. The Medium Energy Proton Electron Detector (MEPED) measures electron counts in three integral energy channels (>30, >100 and >300 keV) with the nominal upper energy limit of 2.5 MeV. The instrument consists of two telescopes, T0, that views radially outward along the Earth-satellite axis, and the other, T90, which is mounted perpendicular to it. Since the satellite's orientation with respect to the Earth is unchanged along the orbit, its orientation with respect to the magnetic field lines changes significantly. This results in both detectors observing electron populations in the bounce and drift loss cones, as well as trapped electrons, at various points across the orbit. According to Rodger et al. (2010b), for $L > 1.4$, the electrons detected by the T0 telescope are mostly inside the bounce loss cone. The T90 telescope usually measures a combination of electrons in the drift and bounce loss cones, as well as trapped electrons, as described by Rodger et al. (2010a). The energetic electron channels on the POES SEM-2 instrument are strongly affected by proton contamination, especially during disturbed geomagnetic conditions (Kp > 4) (Rodger et al., 2010b). For example, the percentage of contamination for the first channel (>30 keV) and T0 telescope is 24.7 % during quiet conditions (AE ≤ 150 nT), 20.6 % during disturbed conditions (AE > 150 nT), and 22.7 % on average. Furthermore, it was found that radiation damage had degraded the POES instrument even within 2–3 year after the launch (Asikainen et al., 2012; Asikainen and Mursula, 2011; Galand and Evans, 2000; Sandanger et al., 2015). A degradation correction could improve the accuracy of long-term comparisons with POES, and is an interesting direction for future investigations.

2.3. GOES

To set up the outer boundary condition for the simulations, we use the data from two spacecrafts at geosynchronous orbit, GOES-13 and GOES-15. These satellites measure electrons in several integral, omnidirectional flux channels using the Energetic Proton, Electron, and Alpha particle Detector (EPEAD) (Rodriguez et al., 2014), and differential pitch angle resolved flux using the Magnetospheric Electron Detector (MAGED) (Sillanpää et al., 2017). We assume exponential dependence of flux on energy to convert integral fluxes from the original integral EPEAD energy channels (>0.6, >2, >4 MeV) to differential fluxes in energy, and assign single values to represent the MAGED energy channels in our processing. To approximate pitch angle distribution, we propagate the pitch angle distribution from the highest energy MAGED channel (458 keV) to all EPEAD energies (0.8–10 MeV).

2.4. SSUSI

SSUSI is an instrument installed onboard Defense Meteorological Satellite Program (DMSP) Block 5D3 satellites (Paxton et al., 2018), aiming to measure chemical and physical properties of the upper atmosphere (above 80 km). The satellite orbit is low-altitude, near-polar, sun-synchronous. Observations are conducted in the far ultraviolet wavelength range 115–180 nm, at 5–8 h universal time (UT) and are able to detect auroral emissions, which are further used to estimate ionization rate. The observations are taken over a swath around 3000 km wide with a nadir pixel resolution of 10x10 km (Paxton et al., 1992, 2017). The average electron energy and energy flux are determined for each pixel from the N2 Lyman-Birge-Hopfield emissions (e.g., Knight et al., 2018).

2.5. AIMOS

The Atmospheric Ionization during Substorm (AIMOS 2.1-Aisstorm) model is a successor of the Atmospheric Ionization Module Osnabrück (AIMOS) model, which provides electron fluxes and ionization rates, that we use for comparison. For details see Section 3.11.

3. Methods

3.1. VERB-4D

For all missions, we use the the International Radiation Belt Environment Modeling (IRBEM) library (Boscher et al., 2022) to calculate adiabatic invariants μ, K, and L^* (Roederer, 1970), using the International Geomagnetic Reference Field (IGRF) internal field model, and the T89 external field model (Tsyganenko, 1989). Closer to the Earth, the shape of the magnetic field is mainly determined by the internal field. Thus, choice of the external field model does not significantly change the values of adiabatic invariants.

We model the dynamics of electrons drifting around the Earth under the action of electric and magnetic fields using the Fokker-Planck diffusion equation (Schulz and Lanzerotti, 1974):

$$\frac{\partial \bar{f}}{\partial t}+\sum_{i}\frac{\partial}{\partial J_i}\left[\left(\frac{dJ_i}{dt}\right)\bar{f}\right]=\sum_{ij}\frac{\partial}{\partial J_i}\left[D_{ij}\frac{\partial \bar{f}}{\partial t}\right], \quad (1)$$

in which $\bar{f}$ is the phase-averaged particle distribution function, or phase space density (PSD), J_i corresponds to the adiabatic invariants, D_{ij} to the diffusion coefficients, t is time. The equation can be transformed into the L-shell, pitch angle, and momentum form by including the appropriate Jacobians. To perform the computations in the most efficient way, we have to solve the equation on a preferably orthogonal grid, which could be achieved by solving the modified Fokker-Planck equation with the additional advection terms (Aseev et al., 2016; Shprits et al., 2015):

$$\frac{\partial f}{\partial t}=-\langle v_\varphi\rangle\frac{\partial f}{\partial \varphi}-\langle v_{R_0}\rangle\frac{\partial f}{\partial R_0}+\frac{1}{G}\frac{\partial}{L^*}G\frac{\partial}{\partial L^*}G\langle D_{L^*L^*}\rangle+$$
$$+\frac{1}{G}\frac{\partial}{V}G\left(\langle D_{VV}\rangle\frac{\partial f}{\partial V}+\langle D_{VK}\rangle\frac{\partial f}{\partial K}\right)+\frac{1}{G}$$
$$\times\frac{\partial}{K}G\left(\langle D_{KV}\rangle\frac{\partial f}{\partial V}+\langle D_{KK}\rangle\frac{\partial f}{\partial K}\right)-\frac{f}{\tau}, \quad (2)$$

where f is the PSD; t is time; φ is MLT, R_0 is the radial distance from Earth in Earth radii; G is the Jacobian of the transformation from a system of adiabatic invariants to a system of modified adiabatic invariants (Subbotin and Shprits, 2012); V, K and L^* are the modified adiabatic invariants. V and K are connected with the first adiabatic invariant μ as follows:

$$V=\mu\cdot(K+0.5)^2; \quad (3)$$

and L^* is connected with the third adiabatic invariant Φ as follows:

$$L^*=(2\pi M)/(\Phi R_E), \quad (4)$$

where M is the magnetic moment of the Earth's dipole field, and R_E is the Earth's radius.

The electron lifetime associated with the loss to the loss cone and magnetopause shadowing is indicated as τ; $\langle v_\varphi\rangle$ and $\langle v_{R_0}\rangle$ are bounce-averaged drift velocities; $\langle D_{L^*L^*}\rangle$, $\langle D_{VV}\rangle$, $\langle D_{VK}\rangle$, $\langle D_{KV}\rangle$, $\langle D_{KK}\rangle$ are bounce-averaged diffusion coefficients.

To perform a full-diffusion modeling, we need a boundary condition, which is pitch angle resolved. In order to assign pitch angle distribution to the Denton model to set up boundary conditions, we assume electron flux follows a sine distribution in equatorial pitch angle. The model is recommended to be used for times when the magnetosheath moves outward of GEO orbit including only the effects of storm dynamics. The Denton model accounts for electrons with energies from ~40 eV to 40 keV. In order to extend the energy domain above 40 keV and accurately model the substorm dynamics, we use observations of fluxes from GOES satellites. We review the importance of boundary conditions for the simulations in detail. We perform a sensitivity study using three different boundary conditions (Section 3.7), showing that the model is highly sensitive to the choice of boundary condition, and use the results of the study to choose one that improves agreement with satellite observations.

We set our model on a four-dimensional grid of modified adiabatic invariants $PRVK$. We set the model grid resolution to 0.5 h in MLT, which allows to cover 49 points on the P grid. We set the grid resolution 0.2 R_E in radial distance R from 1 to 6.6 R_E, which covers 29 points. The lowest energy on the V grid is 200 eV and the highest is 10 MeV, where we set up the flux to be zero. The energy grid allows us to cover all ring current energies and particle populations relevant to modeling of the ring current. The usage of an energy value lower than 10 MeV or consideration of high energetic particles requires to set up accurate

boundary fluxes that are also energy dependent. Setting the upper energy boundary significantly above ring current energies (200 eV – 500 keV) ensures that the simulation is not sensitive to the exact definition of the boundary. The V grid is logarithmic and resolves 100 points in energy, which allows us to decrease the appearance of numerical artifacts at high energies seen on grids with lower resolution, and computationally fast at the same time. On the K grid, we cover all pitch angles from 0.3° to 89.3°. The K grid resolves 101 points and is logarithmic, which allows us to have more points inside the loss cone, and reproduce loss cone particle dynamics more accurately.

As a starting point, we run a short-term simulation, and validate the results for two particle populations, one trapped in the magnetosphere and the other precipitating to the atmosphere. We calculate ionization rates and compare them to two existing ionization rate data sets, both based on the satellite data. Similarly to Aseev et al. (2019), we set the Dirichlet boundary condition for energies: we assume flux to be zero for the highest energy on the boundary, and use the steady state solution of an average spectrum obtained from the Combined Release and Radiation Effects Satellite (CRRES) observations applied to the radial diffusion equation as the lower energy boundary (Shprits and Thorne, 2004). The Dirichlet condition allows us to account for a balance of convective sources and losses of source population. For pitch angles, we use the Neumann boundary conditions with zero derivative of PSD at the lower boundary to account for the presence of particles inside the loss cone and strong diffusion. For the upper pitch angle boundary, we set the Neumann condition, since we want to have a flat pitch angle distribution at 90° and simulate strong diffusion. As we run a short-term simulation, the model cannot reach a realistic state during the event if started from an empty magnetosphere. Thus, we set up the initial conditions from RBSP-B HOPE and MagEIS measurements of PSD during an inbound pass starting on the 16 March 20:00 UT and ending at midnight on the 17 March. We assume symmetry of electron flux in MLT to increase the MLT coverage of the observations, and assign the calculated initial conditions to 16 March 20:00 UT.

3.2. Electric and magnetic field models

Eq. (2) used to model the ring current includes two convection terms, which are responsible for the drift motion of the particles in the radial and azimuthal directions. Drift velocities depend on the field models used to approximate the global electric and magnetic fields. For the electric field, we set up the Kp-dependent Volland-Stern electric field model (Volland, 1973; Stern, 1975; Maynard and Chen, 1975), and the magnetic field configuration is assumed to be a dipole (computationally the simplest). Aseev et al. (2019) compared the model results to the observations using two electric field models, the Weimer (2005) polar cap potential model, and the Volland-Stern electric field model. The second model showed a better agreement with the RBSP observations at high L-shells but did not reproduce the rapid variation of the electric field measured by the Van Allen Probes.

3.3. Diffusion coefficients

The radial diffusion term is included as the third term on the right-hand side of Eq. (2). There are several approaches to modeling the process of radial diffusion. Our approach uses the Brautigam and Albert (2000) Kp-dependent radial diffusion model. This parametrization allows for the good agreement with observations (Drozdov et al., 2017; Drozdov et al., 2021; Wang et al., 2020).

To accurately model local diffusion, which is responsible for both scattering and the acceleration of particles within the inner magnetosphere (e.g., Millan and Baker, 2012; Shprits et al., 2008a; Thorne, 2010), we use a model that includes energy, pitch angle and mixed energy-pitch angle diffusion terms. The diffusion coefficients are calculated using the Full Diffusion Code (FDC) (Shprits and Ni, 2009), based on the field-aligned code (Shprits et al., 2006a) that computes resonance scattering rates. Application of an up-to-date wave model that provides diffusion coefficients for local diffusion terms is essential, as wave-particle interactions are the main mechanism responsible for particle precipitation inside an L-shell of 8 (Ni et al., 2011a, 2011b; Thorne, 2010). We use diffusion coefficients obtained from the wave model by Wang et al. (2019), based on more than 5 years of the Van Allen Probes observations. The regression model of the wave amplitude as a function of Kp, L, MLT and magnetic latitude is constructed as a fit to the root mean square of wave amplitudes and covers all MLTs, L-shells from 3.5 to 6 for Lower Band Chorus (LBC) and from 4 to 6 for Upper Band Chorus (UBC), and is valid for $Kp \leq 6$. The chorus wave model in Wang et al. (2019) is limited to magnetic latitudes up to 20°, due to the orbits of Van Allen Probes. Wang and Shprits (2019) extended the wave model to the middle latitudes 20°–45° referring to the Cluster observations (Agapitov et al., 2018). Using the calculated diffusion coefficients, Wang and Shprits (2019), Wang et al. (2020), Shprits et al. (2022) performed simulations for MeV electrons for a long-term run (from 1 to 5 years) and specific storms using GOES data for the boundary conditions. Their simulation results agree very well with the satellite observations.

We include diffusion coefficients of one of the latest hiss waves model from Orlova et al. (2016), which showed a good performance in numerical simulations (Drozdov et al., 2015; Shprits et al., 2015, Yu et al., 2016). This empirical hiss wave model is based on two years of Van Allen Probes observations. The authors developed a cubic regression model for the average hiss magnetic field intensity based on Kp, L, magnetic latitude, and MLT and compared the results with the spectral distribution and wave amplitude to previous data from the CRRES mission. They

compared two models in a common L-shell sector from 3 to 5.5, for three Kp values, and found that the new model reproduces the observations at energies 150–400 keV and $3 < L < 3.6$. We calculate plasmapause location using the Carpenter and Anderson (1992) model. We use the chorus wave model to describe diffusion outside the plasmapause, and the hiss wave model to describe diffusion inside the plasmapause. Fig. 1 shows energy (D_{VV}), pitch angle (D_{KK}) and mixed (D_{VK}) diffusion coefficients for electrons at 30 keV in radial coordinates (in units of Earth radii from the center of the Earth). Panels (a)-(c) show diffusion coefficients for the lowest Kp value reached over the 3-day period in this study, and Panels (d)-(f) show diffusion coefficients for the highest Kp value. We see a shift of the chorus wave intensity for higher Kp values, from the night-dawn towards the dawn side (for a detailed explanation, see Fig. 13 (l) from Wang et al. (2019). The highest values of the chorus diffusion coefficients are obtained for diffusion in the adiabatic invariant K, indicating that the main wave-particle interaction is pitch angle scattering. The values of the hiss diffusion coefficients are below 10^{-2} everywhere. As we will show later in the Section 4.1,

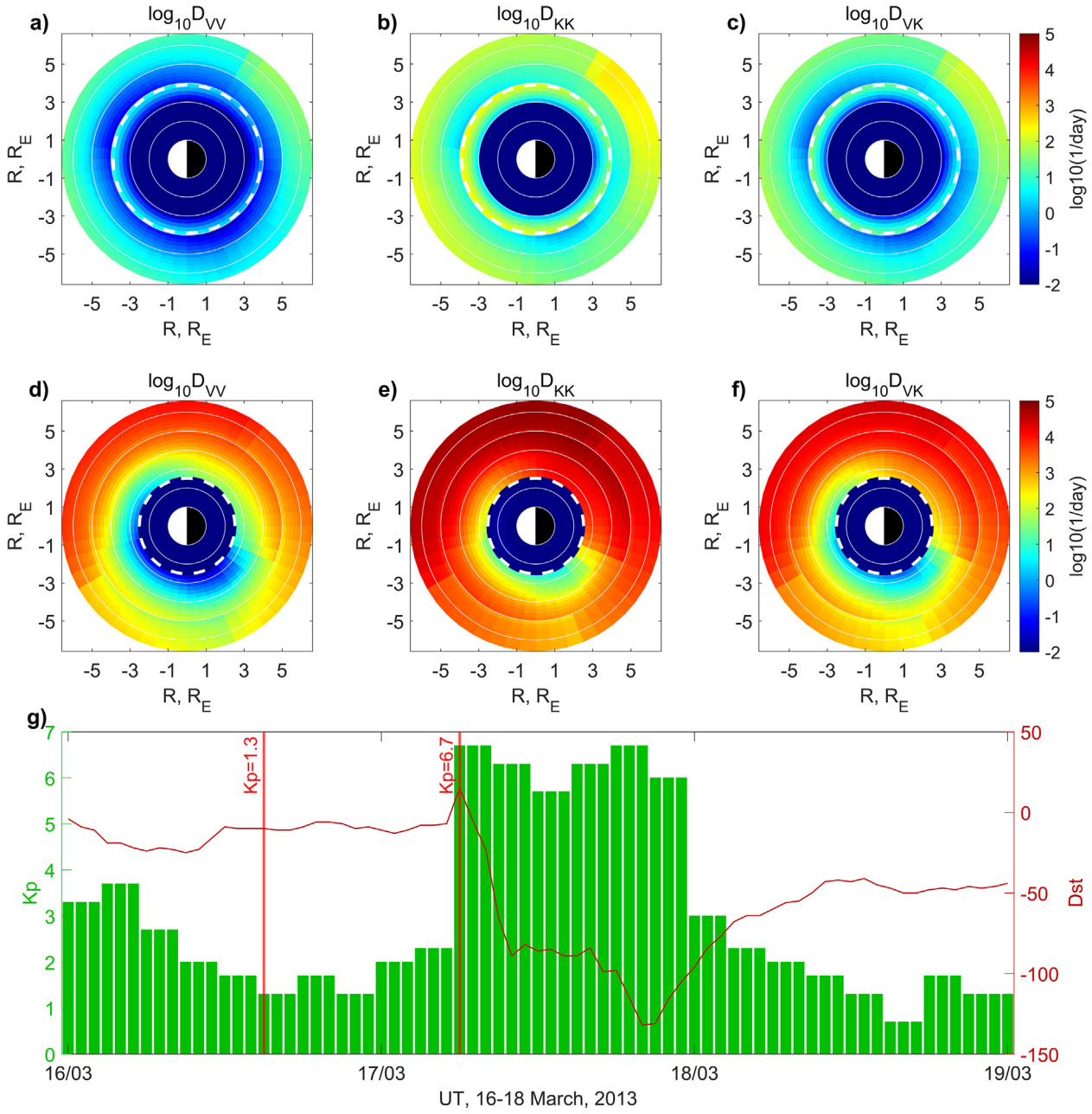

Fig. 1. Diffusion coefficients in the equatorial plane for energy of 30 keV and equatorial pitch angle of 10°, for 16 March 2013 15:00 UT, Kp = 1.7 (Panels (a)-(c)), which value is marked with a red line on the left in Panel (g), and 17 March 2013 06:00 UT, Kp = 6.7 (Panels (d)-(f)), which is the value marked with a red line on the right in Panel (g), transformed into the grid of modified adiabatic invariants V and K. The white dashed line corresponds to the location of the plasmapause.

the spatial distribution of precipitated electron flux is directly connected to the distribution of the chorus wave intensity in space.

3.4. Magnetopause location

Loss to the magnetopause and accompanied outward radial diffusion (e.g., Shprits et al., 2006b) can provide an effective loss mechanism of the radiation belt and ring current electrons. Wang et al. (2020) showed that introduction of the magnetopause loss using the last closed drift shell (LCDS) into the magnetospheric model significantly contributes to the dropouts of electrons at high L-shells up to 6.6. We calculate the LCDS using the Tsyganenko 2004 (T04) model (Tsyganenko et al., 2003; Tsyganenko and Sitnov, 2005). We approximate the effect of magnetopause loss by setting flux at the LCDS to zero in the dayside sector (MLT 9–15 h), which is the closest to the region where the magnetopause crosses the magnetosphere. Development of a more accurate MLT-dependent magnetopause model is left as the subject of a future study. We include this additional loss into our modeling to reduce flux values at the high L-shells during the storm main phase.

3.5. Comparison with RBSP observations

The VERB-4D code provides PSD on a four-dimensional grid of modified adiabatic invariants as an output. To convert it into flux, we multiply modeled PSD by a square of momentum times the speed of light pc. For each L we interpolate the flux for a specific energy and pitch angle searching for the nearest value on a 2D grid. To compare the gridded flux to the flux, measured by satellites at certain location in space, we have to conduct a "flyby" – an approach that allows to obtain pitch angle and energy resolved flux for a specific position that corresponds to the satellite's position. For that, we choose two sequential points in time from the model, and select all satellite observations in this interval. Then we conduct sequential linear interpolation in time from the VERB-4D times to the times of the measurements, from the VERB-4D P to the satellite's MLT positions, and then from the VERB-4D R values to the satellite's L positions.

To quantify the difference between the Van Allen Probes observations and modeled flux, we use the normalized difference (Drozdov et al., 2021), which is calculated using the following formula:

$$ND_{max}(l^*,t) = \frac{J_O(l^*,t) - J_S(l^*,t)}{max|_{over\ L^*\ every\ 8\ hours} \frac{J_S(L^*,T)+J_O(L^*,T)}{2}}, \quad (5)$$

where J_O is observed flux, J_S is simulated flux, t and l^* are corresponding time and L^* for observed and simulated points; T and L^* are the sets of all the times and all the L^* that lie within one orbital period (approx. 8 h).

Fig. 2 shows the comparison of the modeled VERB-4D flux and observed by RBSP flux. We see that the agreement between the model and the observations is better for higher energies. We made a "flyby" of RBSP satellites through the model, and calculated the mean value of the ratio between observed and modeled flux. Panel (d) shows that for 32.6 keV the model overestimates the flux by 10.13% during the recovery phase of he storm for $R > 3$. The decrease in the flux (see dark blue portion of curve) along the orbit flyby are caused by the numerical instabilities that are due to simultaneous action of convection and diffusion. For the energy of 94.1 keV the normalized difference is 8.14%, which is the least value among the three energies. A comparison of the model and observations for the energy of 300 keV shows a moderate overestimation at $R = 4 - 6$ R_E. The normalized difference for the energy of 303.4 keV equals to 13.25% and is the greatest among the three energies.

3.6. Comparison with POES observations

We compare the modeled precipitated fluxes and POES observations. We add a processing step to restrict ourselves strictly to observations of precipitating fluxes for more accurate comparison. According to Li et al. (2013), the central pitch angle measured by the POES SEM-2 detectors corresponds to the centre of the telescope field of view. Taking into account that the detector's opening angle is 30°, we can select only those particles whose maximal equatorial pitch angle lies within the loss cone for T0, and those particles whose minimal equatorial pitch angle lies outside the loss cone for T90. Then, we calculate the equatorial pitch angle from the conservation of the first adiabatic invariant for two points:

$$\alpha_{eq} = sin^{-1}\left(\sqrt{\frac{B_{eq}}{B_{POES}} sin(\theta \pm \beta)}\right), \quad (6)$$

where B_{eq} is the magnetic field strength at the equator, B_{POES} is the magnetic field strength calculated using the IGRF model (Thébault et al., 2015) at the satellite location, and θ represents the central pitch angle of the POES detector, which is supplied with the data. β denotes the half-angle of the detector's acceptance, which is set at 15° for the POES telescope. The loss cone is dipole and is defined as follows:

$$\alpha_{LC} = sin^{-1}((4L^6 - 3L^5)^{-1/4}), \quad (7)$$

where L denotes L-shell. We compare the VERB-4D output to the satellite observations by interpolating the model output to the time and location of the measurements. We transform PSD into flux using an approach, described in the previous section, and interpolate it on the energy range, which lowest value corresponds to the certain energy channel and the highest value is 2.5 MeV. We interpolate the flux on an equatorial pitch angle from POES, which is calculated from the central pitch angle using Eq. (6), for one time point. We apply the same "flyby" procedure, as described in the Section 3.5. The POES SEM-2 flux mea-

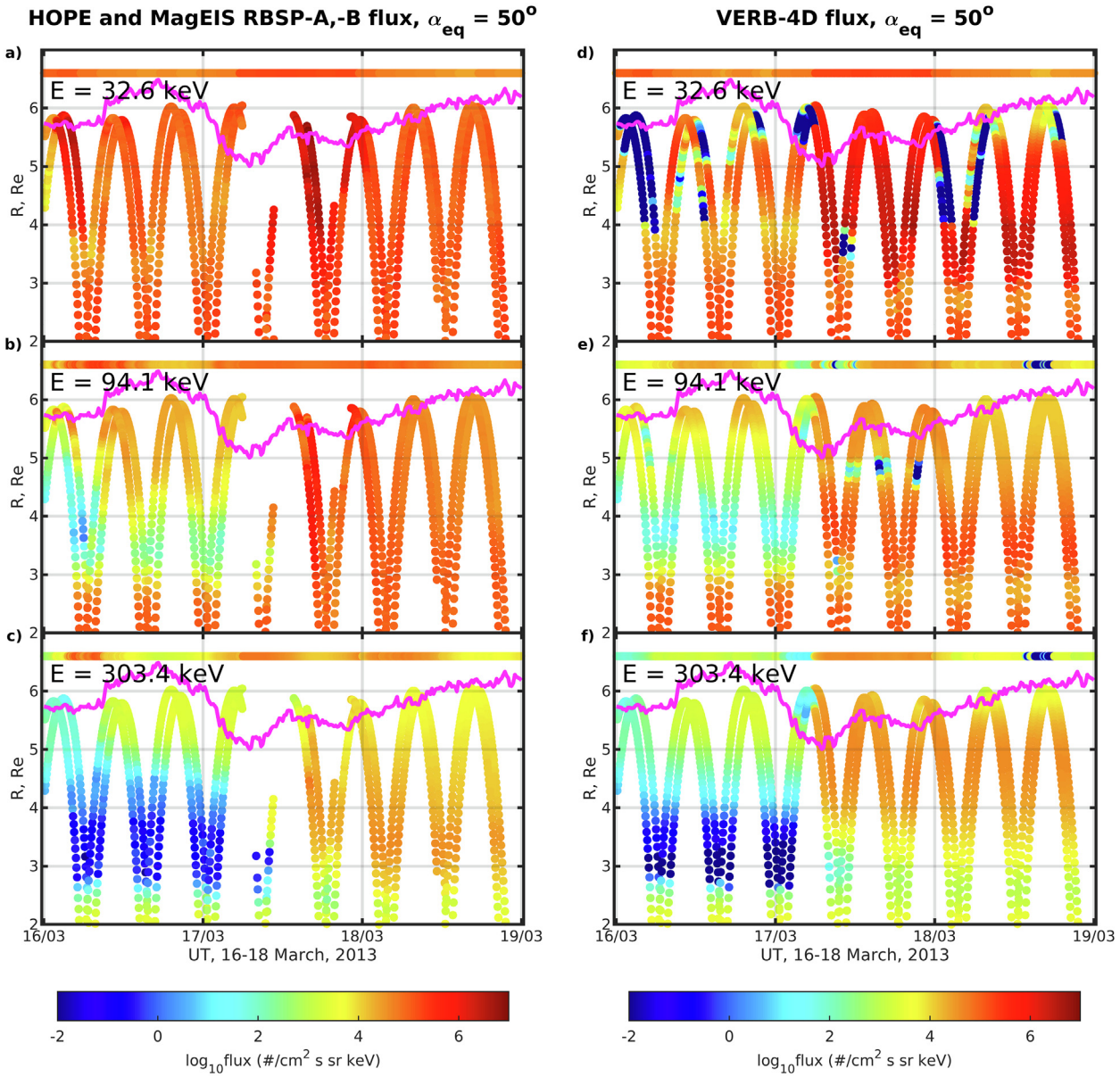

Fig. 2. Electron fluxes as a function of time and radial distance for three energies, at equatorial pitch angle of 50°. Van Allen Probes A and B spacecraft HOPE and MagEIS observations, Denton et al. (2015) boundary fluxes (Panel (a)) for energy of 32.6 keV, and GOES-13 and GOES-15 observations, which fluxes are adiabatically transformed to 6.6, for energies of 94.1 and 303.4 keV (Panels (b), (c)). VERB-4D simulations of the flux evolution for energies 32.6, 94.1 and 303.4 keV (Panels (d), (e), (f)), made at the location of the spacecrafts. The magenta lines represent the location of the magnetopause calculated using the LCDS.

surements are provided with integral energy channels, thus we need to apply an additional processing step to the modeled fluxes. We integrate the model output over the energy range, in the anisotropic case:

$$J(E > E_{th}) = \int_{E_{th}}^{E_{max}} J_{eq}(E)dE, \quad (8)$$

where E_{max} is 2.5 MeV, and E_{th} is the lower bound of the energy channel (30, 100, 300 keV) that corresponds to one of the POES SEM-2 channels.

According to Rodger et al., (2010a), near the equator, the T90 telescope measures fluxes inside the bounce loss cone (BLC), but in other areas it measures a mixture of other populations, both trapped fluxes and fluxes inside the drift loss cone (DLC). Near the South Atlantic Anomaly (SAA), the instrument detects a mixture of DLC, BLC and trapped populations, though most of the flux comes from DLC electrons. The T0 telescope measures DLC and BLC populations near the equator, and only BLC closer to the poles. We apply the particle populations separation and make sure to only use BLC particles from T0 for comparisons with modeled precipitating flux, and

trapped particles from T90 for comparisons with modeled trapped flux. This procedure of separating particle populations is described in more detail in Shprits et al. (2023). We define BLC as points where magnetic field strength at the mirror point of a particle is equal to or greater than the magnetic field strength at the footpoint of the field line. DLC is defined using the minimum of the magnetic field strength at the footpoint (100 km). All other particles are assumed to be trapped.

The continuous values of the POES observed flux plotted against L lie above the level $10^{2.5}$ 1/(cm^2 s sr), which is taken as a noise threshold level from analysis of flux distribution depending on L (Fig. S1 from the supplementary material). Simulations and tests show that the measurements of electrons with energy levels > 30 keV, >100 keV, and > 300 keV are affected by contamination from protons with energy levels ranging from 210 to 2700 keV, 280–2700 keV, and 440–2700 keV, respectively (Evans and Greer, 2000). Yando et al. (2011) determined the crosstalk sensitivity by Geant4 simulations and get similar numbers only with an upper energy threshold of 2600 keV. Since the proton energy spectrum is unknown, certain assumptions need to be made in order to eliminate this contamination. We estimate the proton energy spectrum, according to Lam et al. (2010). The method assumes that the spectrum consists of a series of piecewise exponential functions within each measured proton energy channel range. We initially define these functions using a bow tie method (Selesnick and Blake, 2000), and then iterate to improve our understanding of the spectrum. By subtracting the resulting proton counts from the electron counts, we obtain the corrected electron counts for each energy channel.

The storm under study is accompanied by a solar proton event (SPE), and the electron instrumentation could be affected by the penetrating energetic SPE protons (Evans and Greer, 2000; Yando et al., 2011). To prevent the SPE from affecting the study, we remove measurements affected by it during the satellite data processing according to the NASA SPE catalog (NASA, 2023).

3.7. Model sensitivity to boundary conditions

We assume complete loss of particles into the atmosphere at that boundary (PSD at the inner L boundary is zero). The outer L boundary condition is adapted from the combination of the Denton et al. (2015) model using GOES-13 and GOES-15 observations. To combine observations from two GOES satellites, we take a mean value of their fluxes. The empirical Denton model is based on 82 years of observations from different satellites at GEO operated by the LANL, and provides Kp, Local Time (LT), and energy dependent ion and electron fluxes at the geosynchronous orbit. It covers energy range from 1.8 eV to 40.7 keV. We assume sinusoidal pitch angle distribution to obtain the directional flux. To account for sharp Kp drops during this extreme event, we apply additional smoothing by fitting the flux as a 7th order polynomial in Kp. To construct a boundary condition from the GOES observations, we adiabatically transform fluxes from GOES-13 and GOES-15 L-shells to $L^* = 6.6$ for each time point assuming a flat PSD distribution in L. First, we calculate the momentum multiplied by the speed of light (pc) value measured in MeV from the values of energy, measured by GOES:

$$\mathrm{pc_{GOES}} = \sqrt{\left(\frac{\mathrm{E_{GOES}}}{\mathrm{mc^2}}\right)^2 - 1} \cdot \mathrm{mc^2}, \tag{9}$$

where pc_{GOES} is pc for all GOES energies, E_{GOES}, provided in the GOES dataset, m is the electron mass and c is the speed of light.

Then, we transform J measured by GOES into PSD (f), using the pc values obtained from Eq. (9):

$$\mathrm{f_{GOES}} = \mathrm{J_{GOES}}/(\mathrm{pc_{GOES}})^2. \tag{10}$$

We calculate the values of pc for $L^* = 6.6$, including a value of the magnetic field strength at $L^* = 6.6$:

$$\mathrm{pc_{GOES,L*=6.6}} = \sqrt{2\,\mu_{\mathrm{GOES}}\,\mathrm{mc^2}\,\mathrm{B(L^* = 6.6)}} \,/\, \sin(\alpha_{\mathrm{eq\,GOES}}), \tag{11}$$

where μ_{GOES} is the first adiabatic invariant and α_{eqGOES} is an equatorial pitch angle calculated with a magnetic field model.

Finally, we obtain flux value at $L^* = 6.6$ by multiplying the known PSD values and the momentum-speed of light value at 6.6:

$$\mathrm{J_{GOES,L*=6.6}} = \mathrm{f_{GOES}} \cdot (\mathrm{pc_{GOES,L*=6.6}})^2. \tag{12}$$

We only apply this transformation for $L^* \geq 5.2$, since in for these L-shells the T89 magnetic field model has been shown to accurately capture the behavior of the real magnetic field. For L^* values lower than 5.2, we linearly interpolate flux in time for each energy and pitch angle.

To construct the combined flux array for the boundary, which is MLT, pitch angle and energy resolved, we use MLT and energy resolved fluxes from the Denton et al. (2015) model for the energies up to 40.7 keV, and pitch angle and energy resolved fluxes from GOES-13 and GOES-15 observations, which were transformed to $L^* = 6.6$ following the algorithm above. If we have flux for a given energy at a given time from both the Denton model and GOES observations, we calculate the average and continue the array from the GOES values for subsequent higher energies. We set up the PSD at the boundary to zero, when magnetopause is inserted inside the model domain and one or two GOES satellites are located inside that area simultaneously.

To test the model's sensitivity to boundary conditions, and find the one maximizing the agreement with observations, we ran three simulations with the same configuration parameters and simulation grid, only changing the bound-

ary conditions. To expand fluxes from MLT and energy resolved fluxes from the Denton model to energies higher than 40.7 keV, we apply linear extrapolation and compare the result to the Van Allen Probes observations.

Fig. 3, Panels (a)-(c) show the Van Allen Probes A and B, HOPE and MagEIS observations for the three energies, and pitch angle of 50°. Panels (d)-(f) show the values of the normalized difference between observed and modeled fluxes, calculated using the Eq. (5). Panels (g)-(i) show the combined GOES-13 and GOES-15 fluxes, that are pitch angle and energy resolved and cover energies from 38 keV up to 10 MeV. We apply linear extrapolation to expand fluxes to energies lower than 38 keV. Panels (j)-(l) show the result of comparison between a run with combination

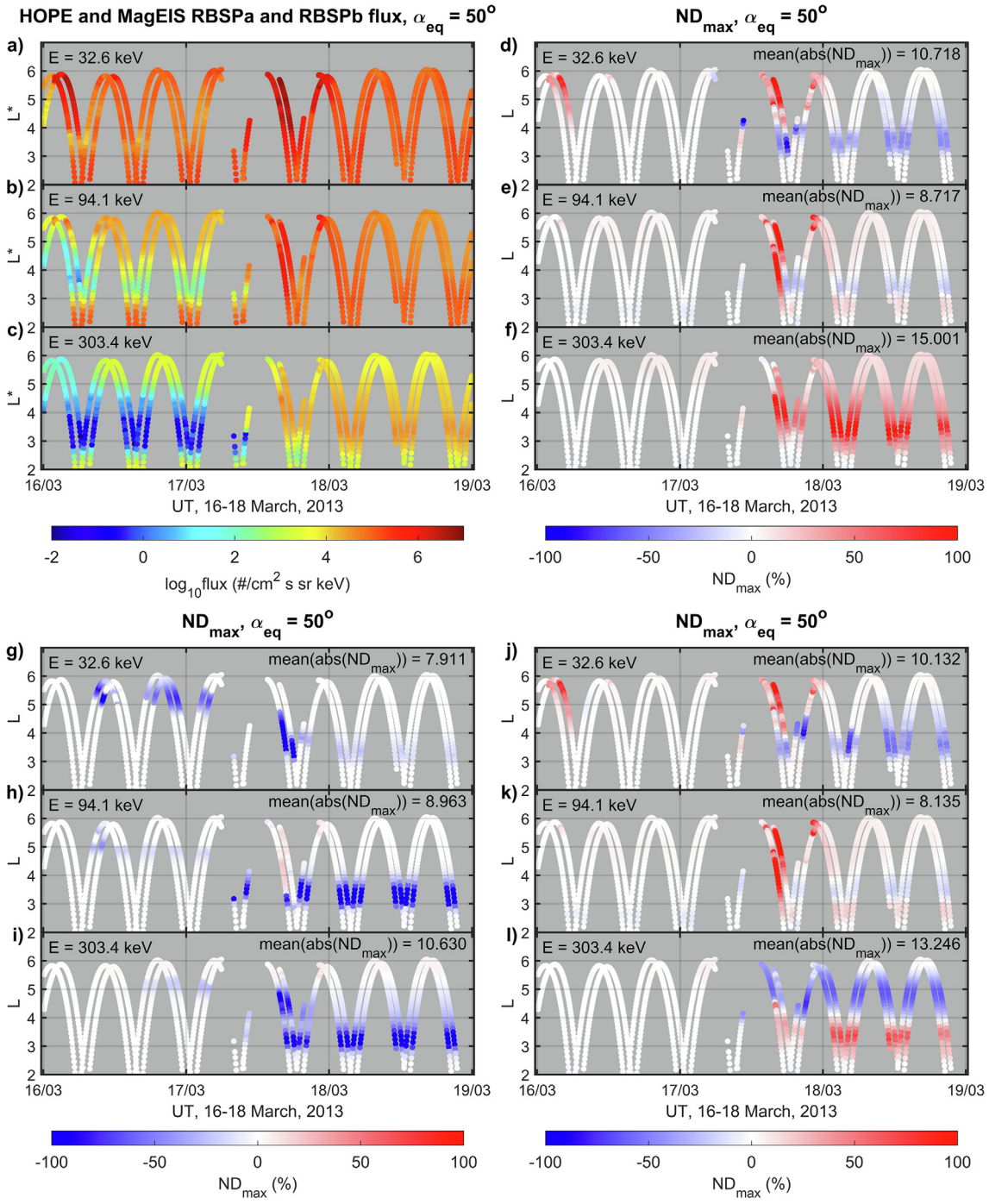

Fig. 3. Van Allen Probes measurements for energies of 32.6, 94.1 and 303.4 keV as a function of time and radial distance (Panels (a)-(c)). Normalized difference between the Van Allen Probes measurements and the VERB-4D model with different boundary conditions for three energies and an equatorial pitch angle of 50°: from Denton et al. (2015) (Panels (d)-(f)), from GOES-13, GOES-15 (Panels (g)-(i)) and with the combined boundary conditions (Panels (j)-(l)).

of the Denton model and GOES boundary conditions and Van Allen Probes observations. An additional plot of the combined flux spectra used in the third case could be found in the supplementary material (Fig. S2).

Usage of the Denton et al. (2015) model for the boundary (Panels (d)-(f)) produces both underestimation and overestimation of observations that is the lowest for the energy of 94.1 keV. The model produces underestimation of observations, which intensifies for higher energies. The highest absolute mean of the normalized difference is reached for the highest considered energy of 303.4 keV and is 15%. The usage of the boundary conditions from the GOES observations (Panels (g)-(i)) oppositely produces overestimation that becomes stronger at the energy of 94.1 keV. GOES boundary conditions overestimate the observations between 3 and 4 R_E. The highest absolute mean of the normalized difference equals to 10.6% and is reached for the highest considered energy. The simulation using the combined boundary conditions (Panels (j)-(l) reduces the discrepancy for the energy of 32.6 keV comparing to the setup with the Denton model. For 94.1 keV, we obtained the lowest absolute mean of the normalized difference among two other setups. The discrepancy fluctuates around zero, except from the setup with the GOES observations, for which it is localized at the region 3–4 R_E. There is also a moderate overestimation for $R > 4$ R_E during the storm main phase for the energy of 303.4 keV. For 303.4 keV, the absolute value of the normalized difference is lower than in the setup with the Denton model, but shows both underestimation and overestimation in different regions. The highest absolute mean of the normalized difference for that case is 13.25%. We choose the combined boundary condition setup for the following study as it provides lower values of the normalized difference than the other two setups, and the errors are spread across the simulation domain rather than are localized at certain distances.

3.8. Calculation of precipitated fluxes

To calculate the differential precipitated flux J_{LC} from the four-dimensional flux J output of the model for each time step, we use the approach described in Lauben et al. (2001). We apply a cosine factor, which adjusts for the area perpendicular to B_0, and integrate the flux over the solid angle that represents the loss cone. Then, we multiply the double integral with a factor g, accounting for the geomagnetic flux tube contraction. After contraction of the trigonometric functions involved, we obtain the following relation:

$$\mathrm{J_{LC}(t,P,R,E)} = \frac{\pi}{\sin^2\alpha_{\mathrm{LC}}} \int_0^{\alpha_{\mathrm{LC}}} \mathrm{J(t,P,R,E,\alpha)}\,\sin 2\alpha\,\mathrm{d}\alpha, \tag{13}$$

where α is the equatorial pitch angle, α_{LC} is the loss cone pitch angle; P, R, E are the values set up on the grid. Then we find the geodetic coordinates of the footpoints of the field lines using the IRBEM library (Boscher et al., 2022), in order to map fluxes from the equatorial plane to the mirror points. We transform the obtained data set of precipitating fluxes given on the VERB-4D grid into the solar magnetic coordinate system, then to the geodetic coordinates, and project fluxes onto the Earth's surface to obtain flux maps. In the next section, we calculate ionization rate maps at different altitudes from precipitated flux maps using a commonly used parameterization, and show the correlation between flux patterns of a certain energy and ionization rate patterns at a corresponding altitude.

3.9. Calculation of ionization rates

We calculate ionization rates from precipitated fluxes J_{LC} using the parameterization for monoenergetic isotropically precipitating electrons as presented by Fang et al. (2010). For the calculation, J_{LC} is provided as precipitated flux maps in hundred energy channels ranging from 10 keV to 1 MeV with an energy bin size of $\Delta E = 10$ keV with a 15 min time resolution. In contrast to the parameterization in Fang et al. (2008), this parameterization does not assume a Maxwellian energy distribution of the precipitated fluxes, and the full energy spectrum of J_{LC} is simulated by VERB-4D. Fang et al. (2010) used two first-principle models, which solve the electron Boltzmann transport equations and calculate the resulting ionization rate profiles. The parameterization was obtained by applying a least square fit to the normalized quantities. The approach is commonly used in atmospheric studies (e.g., it is used by 5 out of 8 ionization rate models discussed in Nesse Tyssøy et al., 2022), and is an accurate and fast computation method for quantification of the atmospheric impact. Comparison with the other methods showed good agreement during both quiet and disturbed geomagnetic conditions, for energies from 100 eV to 1 MeV. The errors could occur at low energies, which are out of the scope of this study. We briefly summarize key points of the approach below.

The total ionization rate q_{tot} for each energy channel can be calculated as:

$$\mathrm{F} = \mathrm{q_{tot}(z)} / \left(\frac{\mathrm{Q_{mono}}}{\Delta\epsilon} \frac{1}{\mathrm{H(z)}} \right), \tag{14}$$

where F is the normalized energy dissipation, introduced in Fang et al. (2008), $H(z)$ is the atmospheric scale height (cm) (Fig. S3 in the Supplementary material), and $\Delta\epsilon$ is the mean ionization energy of air being 35 eV. Q_{mono} is the incident electron energy flux of the respective energy channel, which can be obtained by integration over the precipitated flux:

$$\mathrm{Q_{mono}(E,t)} = \int_{\mathrm{E}}^{E+\Delta E} \mathrm{J_{LC}(E,t)\,E\,dE} = \mathrm{J_{LC}(E,t)\,E\,\Delta E}, \tag{15}$$

where ΔE is the size of each energy bin of 10 keV. As a result of the height dependence, the ionization rates are functions of the vertical height above the surface of the Earth. From the ionization rate altitude profiles for each energy bin (Fig. S4 in the Supplementary material) we see that the peak is shifting to lower altitudes as the incident electron energy is increasing. The higher the electron energy, the deeper electrons penetrate in the atmosphere (Turunen et al., 2009; Wissing and Kallenrode, 2009). For example, the ionization rate profile of the ring current electrons with an energy of 30 keV peaks around 93 km (also slightly dependent on the background atmosphere), whereas electrons with an energy of 300 keV cause maximum ionization rates at about 70 km altitude. Both agrees well to the Geant4 based Monte-Carlo simulation by Wissing and Kallenrode (2009), their Fig. 2, showing a maximum ionization altitude of about 97 km for 30 keV and 72 km for 300 keV.

We use latitude-dependent zonal daily mean values of 16 March 2013 for atmospheric quantities (density, atmospheric temperature, molecular weight, gravitational acceleration) provided by a simulation of the winter 2012/2013 with the atmospheric chemistry-climate model ECHAM5/MESSy Atmospheric Chemistry – fifth-generation European Centre Hamburg general circulation model/Modular Earth Submodel System (EMAC) in the high-top configuration (Sinnhuber et al., 2022). Ionization rate profiles q_{tot} are calculated for all energy bins in the range from 10 keV to 1 MeV. The overall resulting total ionization rate (IR) profiles are calculated as a superposition of all ionization rate profiles:

$$\mathrm{IR}(z) = \sum_{i=1}^{100} q_{tot}(E_i, z). \tag{16}$$

As a vertical coordinate z, 74 levels of the EMAC model in the upper atmosphere mode were used, starting in the thermosphere at a top height of ~220 km down to the Earth's surface.

3.10. Derivation of the ionization rate from SSUSI

SSUSI electron particle observations are provided in the energy range 2–20 keV, which constrains ionization altitudes suitable for comparisons to 100–600 km. These energies and fluxes are used to calculate ionization rate profiles using the parametrization given in Fang et al. (2010), and using US Naval Research Laboratory Mass Spectrometer and Incoherent Scatter radar (NRLMSISE-00) (Picone et al., 2002) as the neutral background atmosphere. By converting the so-derived ionization rate profiles to electron density profiles, they have been validated against ground-based measurements by European Incoherent Scatter Scientific Association (EISCAT) (Bender et al., 2021). Here, we use an empirical parametrization of these ionization rate profiles, binned in MLT and geomagnetic latitude. This parametrization uses Kp, PC, Ap, and F10.7, and the ionization rates used here were produced with the accompanying model code (Bender, 2023), interpolated to the model pressure grid.

3.11. Derivation of the ionization rate from AISstorm

AISstorm is a numerical model of atmospheric ionization rates due to precipitating particles with high spatial resolution and extends its predecessor AIMOS (Atmospheric Ionization Model Osnabrück) (Wissing and Kallenrode, 2009) by separate treatment of substorm periods. AISstorm calculates 3D ionization rates from precipitating protons, electrons, and alpha particles with a 30 min temporal resolution.

The model includes a sorting algorithm to assign observations from polar-orbiting POES and MetOp satellites to horizontal precipitation cells. For this, AIMOS uses the data from the Total Energy Detector (TED) and MEPED detectors. In addition, high-energy protons and alpha particles from the SEM detectors of the GOES satellites are used in the polar cap. The energy range covers 154 eV–50 0 MeV for protons, 154 eV–300 keV for electrons, and 4–500 MeV for alpha particles. Mean flux maps were calculated from 18 years of satellite data (2001–2018) grouped by Kp level, geomagnetic APEX (Richmond, 1995) vs. MLT location with up to 1° latitide vs. 3.75° longitude resolution, and substorm activity. Each flux map represents a typical spatial pattern of particle precipitation for one particle channel on the global map. Typical average flow maps from AIMOS are given in Yakovchuk and Wissing (2019). The effective flow for a 30 min interval is determined by scaling precipitation maps with direct measurements at that time. Considering that only areas with high flux values (e.g. auroral oval) are used for scaling, the influence of noise in real-time data is suppressed. For each spectral interval of particles, the ionization profile is calculated by the Monte Carlo method (Schröter et al., 2006), and the atmospheric parameters were taken from the Hamburg Model of the Neutral and Ionized Atmosphere (HAMMONIA) (Schmidt et al., 2006) and NRLMSISE-00 (Picone et al., 2002) models. The AISstorm data is available at the (Ionization.de., n.d.) website.

4. Results

In this section, we show the results of the modeled flux validation for both trapped and precipitated populations of particles using satellite observations. Then we validate ionization rates calculated from the precipitated flux using two data sets.

4.1. Validation of the precipitated fluxes

Fig. 4 shows the comparison of the VERB-4D electron fluxes with the POES observations as two columns with the flux values and one column with the values of the normalized difference, calculated using Eq. (5) (Panels (c), (f),

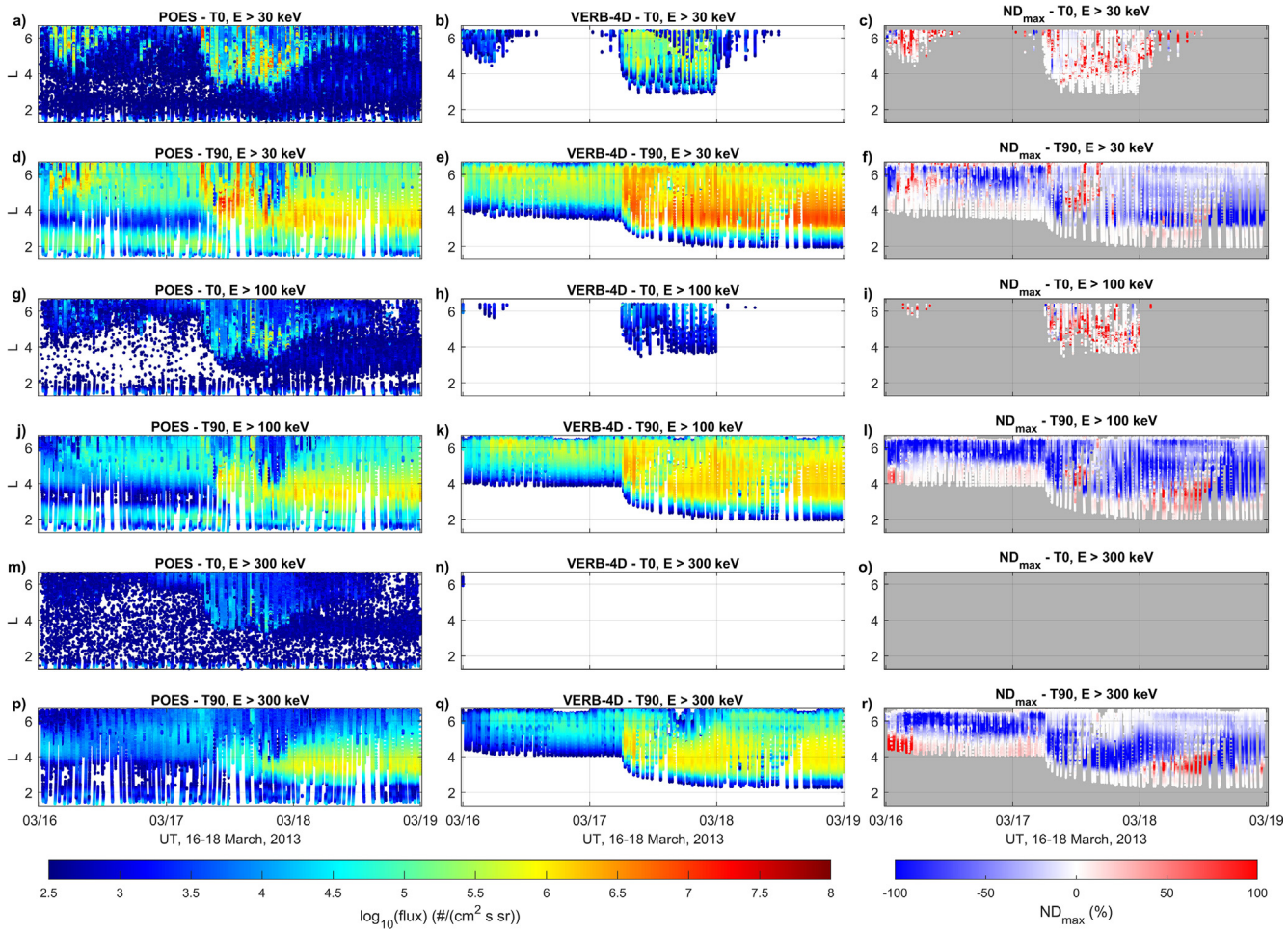

Fig. 4. Integral flux along the POES orbit as a function of time from observations of six POES satellites (Panels (a),(d),(g),(j),(m),(p)), VERB-4D simulation flux (Panels (b),(e),(h),(k),(n),(q)), and normalized difference between POES flux and VERB-4D flux (Panels (c),(f),(i),(l),(o),(r)) for 3 energy channels (>30 keV – Panels (a)-(f); >100 keV – Panels (g)-(l); >300 keV – Panels (m)-(r)) and 2 telescopes (T0 – Panels (a),(b),(c),(g),(h),(i),(m),(n),(o); T90 – Panels (d),(e),(f),(j),(k),(l),(p),(q),(r)). Noise threshold level and particle population separation are applied, as described in the Section 3.6.

(i), (l), (o), (r)). POES T0 flux shows a similar pattern of flux intensification for all three energies. Panel (a) shows two injections, the first of which occurred on March 16 and reached L = 4, and the second of which occurred after flux decay on March 17 and reached L = 3. The second injection has a two-peaked structure that is due to a double Kp jump up to 6.7 on March 17. Panels (g), (m) show that many flux values lie below the noise threshold level. POES T90 flux (Panel (d)) shows two injections originating from the outer boundary and occurring on March 16 and 17. The dark blue areas accompanying the injections correspond to magnetopause shadowing. The area of lower flux extends up to L = 4. A belt-shaped structure at L = 2–3 is attributed to proton contamination from the inner radiation belt. Panels (j) and (p) depict flux intensification starting at midday on March 17, covering L regions from 3 to 5. The model produces significant overestimation for the lowest energy channel (Panels (d), (e)). Moderate overestimation is produced by the model for the second energy channel (Panels (j), (k)). And the best agreement between observations and the model is obtained for the third energy channel (Panels (p), (q)). Trapped fluxes are reproduced more accurately for higher energies (>100 keV), which is also seen in comparison to Van Allen Probes observations on Fig. 2. The modeled pre-storm fluxes underestimate observed fluxes, which could be caused by using initial conditions not accurately reproducing fluxes for low pitch angles. The enhancement during the storm main phase is reproduced quite well, and the absolute mean value of the normalized difference is 17.63% at lowest among all satellites (see Table S1). Precipitated flux is the most intensive and has the best agreement with observations for the first energy channel (Panels (a), (b)) with the absolute mean value of the normalized difference of 11.37%. We see a significant decay of flux and underestimation produced by the model for the second energy channel (Panels (g), (h)) with increase of the absolute mean value of the normalized difference (17.48%). For the > 300 keV energy channel, POES observes electron fluxes that are only slightly higher than our chosen noise threshold level. Although VERB-4D produces significantly lower values than POES for > 300 keV, the location of the flux injection corre-

sponds to the observations (Fig. S5 from the supplementary material), which happens without applying the noise threshold level. Regarding the precipitating particle population, fluxes have a better agreement for lower energies, which contribute most to the total ionization rate value. Thus, we assume that the overall resulting total ionization rates, which are dominated by the impact of the lower energies, are estimated correctly; however we would expect an underestimation of the ionization rates at lower (mesospheric) altitudes due to the underestimation of the higher energies fluxes particularly in the POES T0 telescope. Possible explanations for the discrepancy are presented in Section 5. Quantitative estimation of agreement between the observations and the model is presented as normalized difference in the supplementary material (Table S1).

We also compare our simulation results to the VERB-4D modeled fluxes obtained in Shprits et al. (2015), where the authors simulated the same 17 March 2013 storm using an earlier version of the code with convection, radial diffusion, and energy diffusion. The diffusion coefficients are calculated as described in Subbotin et al. (2011) and are computed using the FDC. Chorus and hiss waves models include both Ultra Low Frequency (ULF) and Very Low Frequency (VLF) waves. Usage of these coefficients produces overestimation of trapped fluxes and underestimation of precipitating fluxes, when compared to the POES observations (Fig. S6 from the supplementary material). Thus, we conclude that usage of a model with latitude dependent chorus wave model is essential for accurate modeling of precipitation.

Fig. 5 shows the distribution of precipitated flux for the three energies at various phases of the storm event. For the energy of 30 keV (Panels (a)-(d)), the flux peaks at the night-dawn side between 4 and 5 R_E, which is associated with the highest value of the pitch angle diffusion coefficients for $Kp > 6$. In that region, there is significant low latitude chorus waves activity, as we show on Fig. 1, which is responsible for the increased electron scattering. For higher energies (Panels (e)-(h), (i)-(l)), we see that the peak of the precipitated flux is shifting towards the dayside. Wang and Shprits (2019) illustrated that there is a different energy dependence of the low- and high-latitude chorus wave pitch angle diffusion coefficients. On the dayside, chorus waves can extend to higher latitude, providing more efficient scattering of higher energy electrons (Wang et al., 2019).

4.2. The effect of precipitation on the particle induced ionization rates

Fig. 6, Panel (a) and (c) show the calculated precipitated flux and Fig. 6, Panel (b) and (d) show ionization rates at two time points. We show ionization rates at the altitude of 93.2 km on Panels (b) and (d) due to a fact that contribution of the 30 keV channel to the overall resulting total ionization rate profile maximizes around that altitude. We see an additional intensification of precipitated flux in the western hemisphere closer to the equator that is caused by an injection of particles from the nightside (see Movie S1 and S2 in the supplementary material). We interpolate obtained rates in geodetic coordinate system that is using the World Geodetic System 1984 (WGS84) reference ellipsoid onto a rectangular grid with the horizontal EMAC grid resolution T42 of about 2.8° × 2.8° in latitude and longitude. We compare and validate this data set of evenly distributed in space ionization rates against the previously obtained ionization rate data sets. The obtained data set could be further used as an input for the atmospheric models as the upper boundary condition.

4.3. Validation of ionization rates

Fig. 7 shows the comparison of calculated ionization rates from precipitated electron fluxes as simulated by the VERB-4D model with SSUSI and AISstorm ionization rates at an altitude of about 93 km for the two time points, 16 March 15:00 UT and 17 March 06:00 UT, corresponding to the minimum and the maximum of Kp, respectively (cf. Fig. 1 and Fig. 6). First of all, we should note that this altitude is already slightly out of bound for SUSSI covering 2–20 keV and thus having a lower altitude threshold of 100 km. Thus, the SUSSI ionization rates should represent a lower boundary of ionization at 93 km and being about two times smaller than a continuous energy spectrum (see Fig. S4 in the Supplementary Material). VERB-4D ionization rates (Panels (a) and (b) on Fig. 7) are generally lower or equal to ionization rates from SSUSI and lower than those from AISstorm, and their latitudinal extent polewards is limited by the equatorward border of the auroral oval. This is due to the fact that VERB-4D ionization rates only represent the population of precipitating electrons from the radiation belts and ring current restricted to L-shells of 1 to 6.6 with energies from 10 keV to 1 MeV. In contrast, SSUSI (Panels (c) and (d) on Fig. 7) and AISstorm data (Panels (e) and (f) on Fig. 7) also include the electrons precipitating from the magnetosphere regions above $L = 6.6$ and the high-energy part of the aurora, which extends down to this altitude. On Fig. 7, during a period of high geomagnetic activity, we find a good agreement between VERB-4D (Panel (b)) and SSUSI (Panel (d)) ionization rates in the transition region of contributions from the radiation belts, ring current and the aurora at the equatorward edge of the auroral oval. On the one hand, this implies a good spatial agreement; on the other hand, the ionization rates might be slightly underestimated. Note that some data points sharply change to low values at the poleward edges of the VERB-4D data due to setup of the boundary conditions (Section 3.7). The agreement of VERB-4D (Panel (b)) and AISstorm data (Panel (f)) in this region is less pronounced. On the one side, this may be partly attributed to long-term spatial averaging procedure in AIMOS, which is needed to produce a global coverage at high temporal and MLT resolution but tends to reduce the peak heights and broadens the peaks spatially and partly to the wider energy range that includes auroral par-

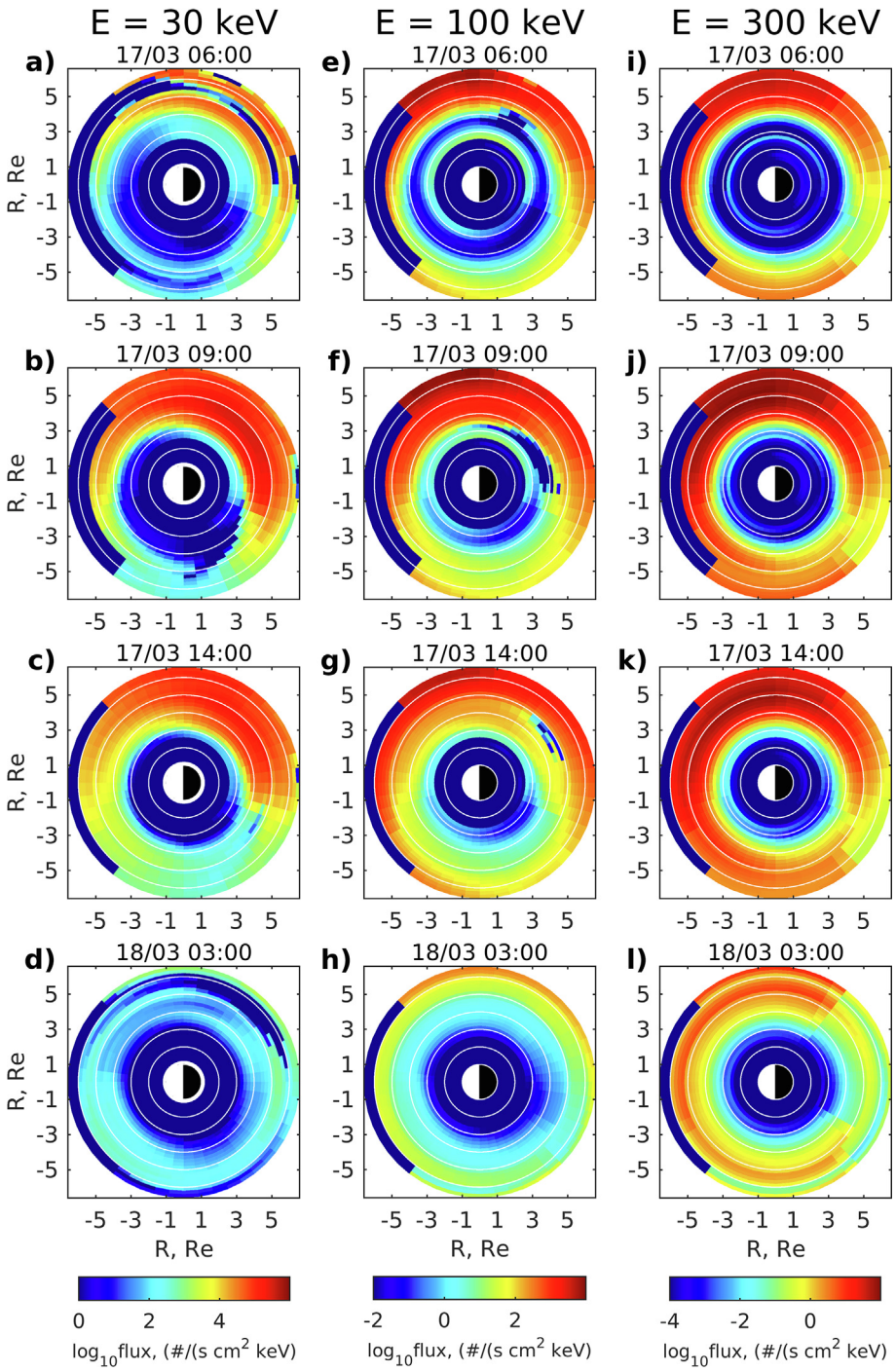

Fig. 5. Radial profiles of precipitated flux for three energies: 30 keV (Panels (a)-(d)), 100 keV (Panels (e)-(h)), 300 keV (Panels (i)-(l)). The plots represent the dynamics of the precipitation process in the equatorial plane through snapshots from the studied event.

ticles down to 150 eV. On the other side, an underestimation of VERB-4D may increase these differences. Interesting is the region of the gap in the auroral oval (longitude of Australia) where there is no strong slope of the ionization rates. Here, VERB-4D and AISstorm agree much better even though VERB-4D derived ionization rates are slightly lower. Similarly, we can see a wide zone (blue) of similar ionization at low Kp in subauroral latitudes where both models agree well. However, it is still unclear if the main differences are due to contribution from low energetic particles or a steep slope as both absent in the noted regions. The overall morphology of SSUSI ionization rates (Panels (c) and (d)) agrees quite well to AISstorm data (Panels (e) and (f)) at this altitude for the two time points.

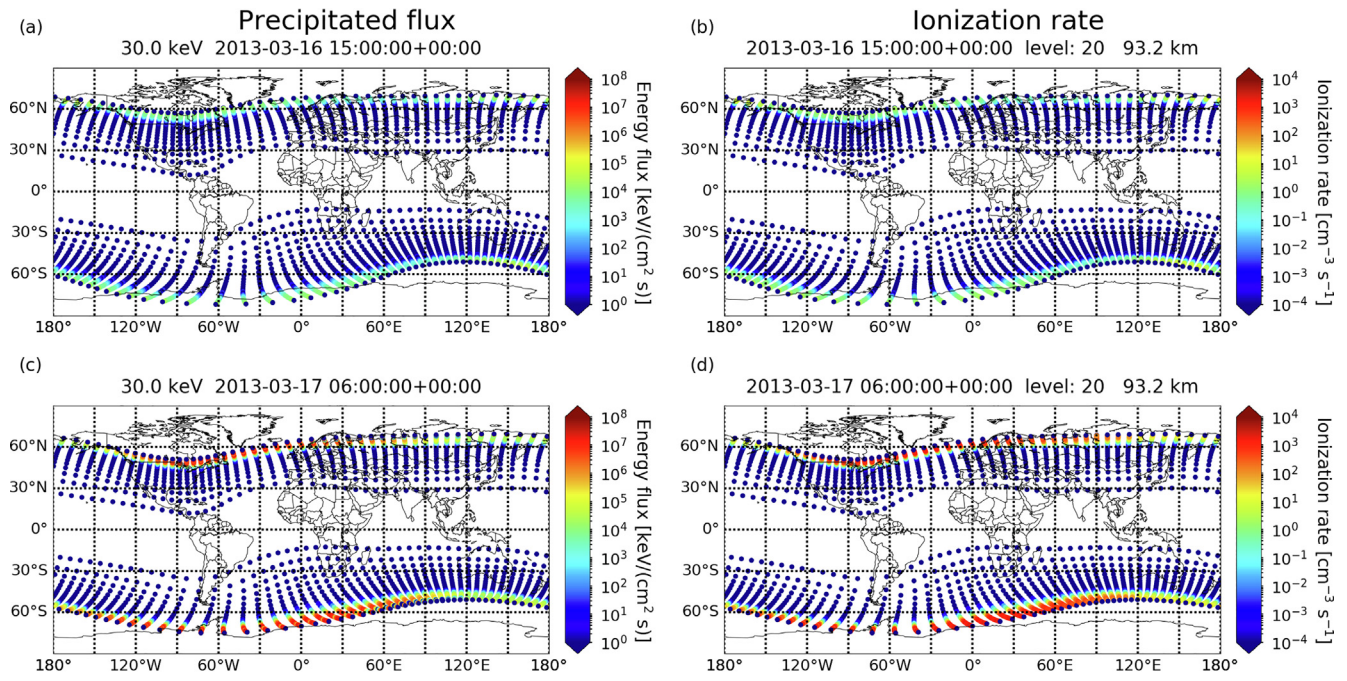

Fig. 6. Energy flux of precipitated electrons at the top of the atmosphere (Panels (a) and (c)) with an energy of 30 keV, and overall resulting ionization rates (Panels (b) and (d)) at an altitude of 93.2 km, mapped onto the Earth's surface for two time points corresponding to Kp = 1.3 (Panels a and b) and Kp = 6.7 (Panels (c) and (d)), respectively. Ionization rates are calculated for energies 10 keV–1 MeV.

Further validations of the ionization rates are left for the future study and could be expanded for a longer period of time.

5. Discussion

In this section, we discuss the possible reasons for the produced underestimation of observed precipitated fluxes by the VERB-4D model at high energies (>300 keV). During the main phase of the storm, we see a sharp decreasing of GOES-13 and GOES-15 *L*-shell position, possibly due to the loss to magnetopause. Adiabatic transformation of the flux observations from GOES orbit to an *L*-shell of 6.6 causes increase in calculated μ, and thus produces higher fluxes, according to Eq. (9), Eq. (10). This causes model overestimation coming from the boundary conditions in comparison to the Van Allen Probes observations. A potential source of error could be the MLT-averaging in the 40.7–300 keV range for GOES derived boundary conditions, where ring current fluxes usually show MLT dependence. In order to extend the boundary that we derived from GOES point measurements to all MLTs, we assume that the flux is the same at all MLTs. Knowledge of the flux distribution in MLT is necessary to account for asymmetry in the ring current, according to the model results.

During this event, only electrons with energies up to 30 keV at $L > 4.5$ and MLT 1–14 h reach the strong diffusion regime during the storm main phase, so for higher energies, the scattering is weaker and is not able to fill the loss cone. The strong diffusion regime is reached due to intense chorus wave activity resulting from the sudden Kp jump from 2.3 to 6.7 during our study period. This is consistent with the results from Meredith et al. (2009), who showed that upper band chorus waves increase loss and cause strong diffusion during periods of high geomagnetic activity in the night and predawn sectors (MLT 21–6 h). The strong diffusion is seen in the model only for energies up to 30 keV (Panel (b) on Fig. 4), meanwhile POES observations show signatures of strong diffusion for all three energy channels during the main phase of the storm for *L*-shells above 3.5 (Panels (a), (e), (i) on Fig. 4). The overestimation of fluxes inside the loss cone in observations could be caused by proton counts detected by the electron detector (>300 keV).

The chorus wave parameterization used in our model has been derived for $Kp \leq 6$ (Wang et al., 2019), but during our study period Kp reaches 6.7 at the time of maximum activity. This could result in underestimation of the diffusion coefficients, leading to an underestimation of precipitating flux. The underestimation of loss can also come from underestimation of the intensity of chorus waves at high latitudes.

Additionally, the underestimation produced by the model as seen on Fig. 4, Panels (f) and (j), could also be caused by non-linear processes occurring inside the loss cone, which our approach cannot accurately reproduce. For example, microbursts can produce non-linear scattering and rapidly fill the loss cone at 300 keV (Chen et al., 2021). Mozer et al. (2018) found correlation between lower band chorus wave activity and microburst precipitation using Van Allen Probes B and AeroCube 6-B (AC6-B)

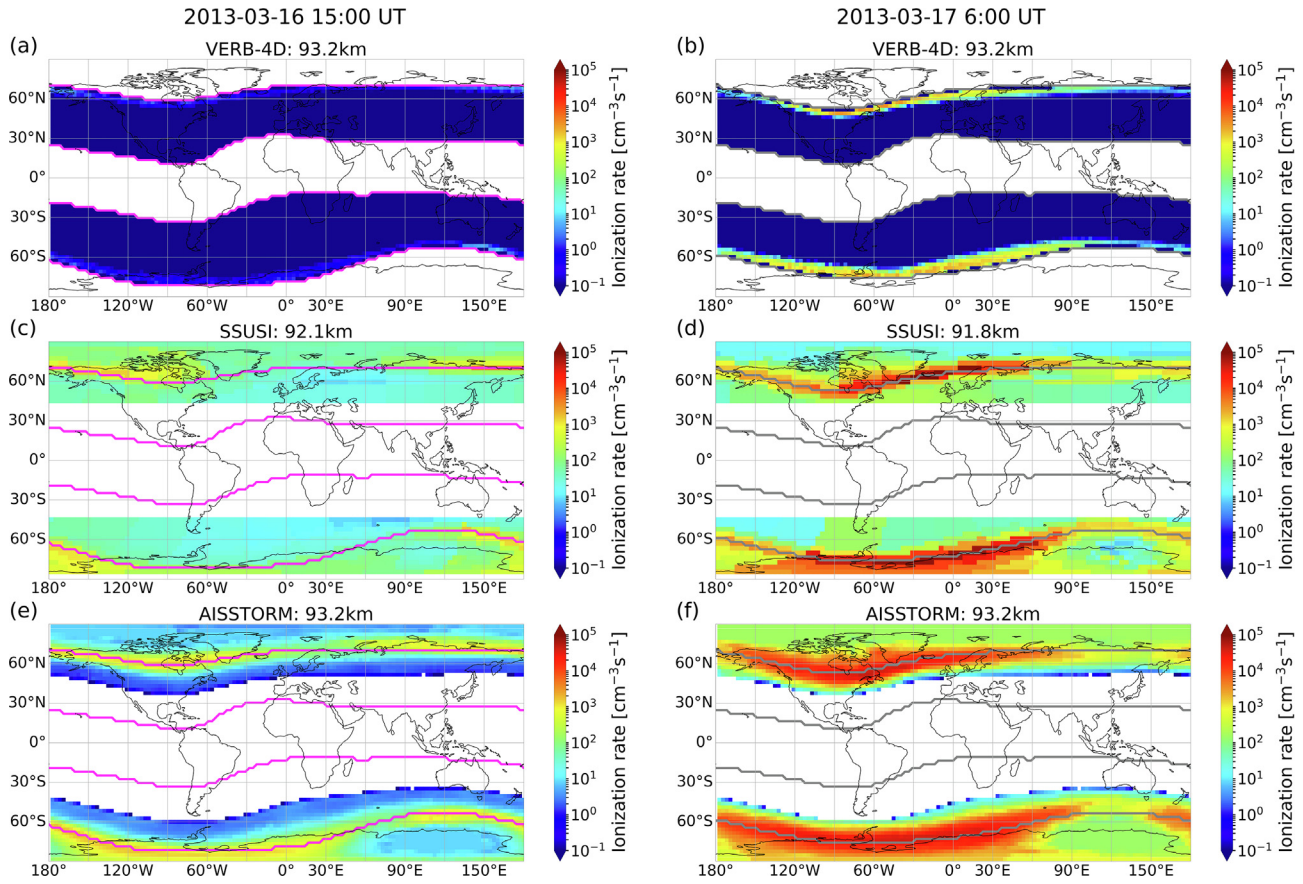

Fig. 7. Comparison of ionization rates (IR) produced with the VERB-4D model (Panels (a) and (b)) to ionization rates observed with SSUSI (Panels (c) und (d)) and modeled with AISstorm (Panels (e) and (f)), for the two time points corresponding to Kp = 1.3 (Panels (a), (c), (e)) and Kp = 6.7 (Panels (b), (d), (f)), respectively. Magenta and gray lines represent the latitude borders of the VERB-4D spatial domain. VERB-4D and SSUSI data have been averaged to the time resolution of AISstorm data of 1 h. The comparison is carried out at an atmospheric altitude of about 93 km.

simultaneous observations. Breneman et al. (2017) found another confirmation of the connection between particle scattering caused by lower band chorus waves and microbursts for energies in the 220 keV–1 MeV range using observations from the Van Allen Probes A and the CubeSat FIREBIRD II satellites.

Another scattering mechanism missing from our current model is wave-particle interactions between electrons and ECH waves, which cause electron precipitation at energies from ~1 keV to tens of keV in the nightside and dawn sectors outside of the plasmapause (Ma et al., 2020; Zhang et al., 2015). Inclusion of these waves into the model could lead to additional scattering of low energy electrons, and consequently higher precipitation fluxes (Haas et al., 2023). Moreover, kinetic Alfvén waves may be another reason for underestimating the loss (Shen et al., 2022), properly accounting for their effects through future work would be a valuable contribution to ring current modeling efforts.

Both the T0 and T90 POES telescopes only cover a part of the loss cone at a time, and they measure different populations as the satellite moves along the orbit. Due to the assumed isotropy of the pitch angle distribution of flux inside the loss cone in models like VERB-4D, there can be significant differences between the model and observations restricted to one part of the loss cone. Nesse Tyssøy et al. (2016) made an attempt to accurately reconstruct loss cone fluxes from MEPED POES observations. From comparison of the observed OH density and modeled OH density from precipitated flux for the reconstructed loss cone in the middle atmosphere, the authors obtained a realistic estimation. Thus, taking into account flux distribution inside the loss cone could lead to more accurate estimations of precipitated flux.

In our model, we assume a dipole magnetic field, and thus do not take into account features of the realistic magnetic field, such as SAA. This introduces another possible source of discrepancy between the model and the observed POES fluxes, since the populations separation procedure applied to the POES data does involve calculation of the realistic drift loss cone using the IGRF magnetic field model. An extension of the model with the IGRF loss cone is left for the future work.

6. Conclusions

In this paper, we present a comprehensive study of the mechanism of the ring current electron precipitation, utiliz-

ing a combination of observational data, theoretical modeling, and numerical simulations to investigate the physical processes that control the precipitation of electrons from the ring current into the atmosphere.

The simulation of the 17 March 2013 storm shows good agreement with the near-equatorial Van Allen Probes observations for the energies higher than 100 keV. Inside the loss cone, the simulation results reproduce the trends observed by POES spacecraft for the energy channels > 30 keV and > 100 keV.

The data set containing the precipitated fluxes for a range of energies from 10 keV to 1 MeV as well as the ionization rates on the EMAC grid has been published with Zenodo (Grishina et al., 2023). We show that the most significant electron precipitation due to chorus waves is found from the nightside to dawn sectors over $4 < L < 5$. From precipitation fluxes we infer an ionization rate data set using the parameterization of Fang et al. (2010) and perform a first comparison to two established ionization rate data sets for two points in time representing high and low geomagnetic activity during our study period. We find promising agreement in the transition region of modeled ring current electron and auroral electron precipitation.

For the future work, maps of projected precipitated fluxes could be used to show how precipitation coincides with the rapidly changing atmospheric parameters. As our ionization rate data set can be used now as an input for atmospheric models, we also will be able to examine the specific impact of electrons from the magnetosphere, in particular ring current electron precipitation on atmospheric chemistry, and better constrain their effect on atmospheric composition. Furthermore, the validation of our derived atmospheric ionization rates with other established data sets demonstrates that our data set could be used in combination with other data sets to quantify the effect of certain electron populations, for example, auroral electrons. We will be able to explore the implications of our findings for understanding the long-term evolution of the Earth's upper atmosphere. Our study represents an important step towards improving our knowledge of the complex interconnection between the Earth's magnetosphere, ionosphere, and atmosphere, and provides data sets that could be used to model and predict the behavior of these systems more accurately in the future.

Data Availability

Processing and analysis of the HOPE and MagEIS data was supported by Energetic Particle, Composition, and Thermal Plasma (RBSP-ECT) investigation funded under NASA's Prime contract no. NAS5-01072. All RBSP-ECT data are publicly available at the LANL website (http://www.RBSP-ect.lanl.gov/). The GOES measurements are available at the NOAA-NGDC website (https://satdat.ngdc.noaa.gov/sem/goes/data/full/). All POES data came from NOAA National Geophysical Data Centre and can be accessed online at https://www.ngdc.noaa.gov/stp/satellite/poes/dataaccess.html. The authors used geomagnetic indices provided by OMNIWeb (https://omniweb.gsfc.nasa.gov/). The IRBEM library can be found under: http://github.com/PRBEM/IRBEM/. The SSUSI data could be accessed at https://ssusi.jhuapl.edu/. AISstorm data is available at https://www.ionization.de/. The Python package to plot the figures is available at https://doi.org/10.5281/zenodo.8216315. The data to reproduce the figures are available at Zenodo repository (https://doi.org/10.5281/zenodo.10046626).

Declaration of competing interest

The authors declare that they have no known competing financial interests or personal relationships that could have appeared to influence the work reported in this paper.

Acknowledgments

This research was supported by the Deutsche Forschungsgemeinschaft (DFG) through the project Understanding the influence of the SPace Environment on Atmospheric CHemistry and dynamics (SPEACH) - SH1206/2-1. This project has received funding from the EU's research and innovation funding programme Horizon 2020 research and innovation programme under grant agreement No. 637302 (PAGER) and the Helmholtz-Gemeinshaft (HGF) [10.13039/501100001656]. Dedong Wang acknowledges the support from the Deutsche Forschungsgemeinschaft (DFG) through the project "Understanding the Properties of Chorus Waves in the Earth's Inner-magnetosphere and Their Effects on Van Allen Radiation Belt Electrons" (Chorus Waves) - WA 4323/5-1. The authors would also like to acknowledge the open access funding enabled and organized by the Projekt DEAL. Alexander Drozdov recieved support under grant number NSF AGS-2211345. Stefan Bender received support from the Birkeland Center for Space Sciences (BCSS), supported by the Research Council of Norway under grant number 223252/F50. Jan Maik Wissing received support from the Deutsche Forschungsgemeinschaft (DFG) under grant number WI4417/2-1.

The Kp index was provided by GFZ Section 2.3 and downloaded from the World Data Center. The authors are grateful to the RBSP-ECT team for providing Van Allen Probes observations data, to the NOAA-NGDC team for providing GOES measurements, and to the NOAA-NCEI team for providing POES data sets. The authors are grateful to Ksenia Orlova for providing the diffusion coefficients used in this study. The authors acknowledge Denis Anikiev for consultation regarding visualization issues. The authors thank Ingo Michaelis, Angelica Maria Castillo Tibocha, Marina García-Peñaranda for useful discussion regarding POES. The authors thank Haley Allison, Michael Wutzig, Julia Himmelsbach and Bernhard Haas for their help in solving the computational issues. The authors acknowledge the devel-

opers of the International Radiation Belt Environment Modeling (IRBEM) library, and the developers of the cartopy library. The interpolations of ionization rate maps to the rectangular horizontal latitude-longitude grid were performed on the bwUniCluster (2.0). The authors acknowledge support by the state of Baden-Württemberg through bwHPC. The authors thank anonymous reviewers for the insightful comments.

Appendix A. Supplementary material

Supplementary data to this article can be found online at https://doi.org/10.1016/j.asr.2024.03.010.

References

Agapitov, O.V., Mourenas, D., Artemyev, A.V., Mozer, F.S., Hospodarsky, G., Bonnell, J., Krasnoselskikh, V., 2018. Synthetic empirical chorus wave model from combined Van Allen Probes and Cluster statistics. J. Geophys. Res. Space Phys. 123, 297–314. https://doi.org/10.1002/2017JA024843.

Angelopoulos, V., Tsai, E., Bingley, L., et al., 2020. The ELFIN Mission. Space Sci. Rev. 216, 103. https://doi.org/10.1007/s11214-020-00721-7.

Aseev, N.A., Shprits, Y.Y., Drozdov, A.Y., Kellerman, A.C., 2016. Numerical applications of the advective-diffusive codes for the inner magnetosphere. Space Weather 14, 993–1010. https://doi.org/10.1002/2016SW001484.

Aseev, N.A., Shprits, Y.Y., Wang, D., Wygant, J., Drozdov, A.Y., Kellerman, A.C., Reeves, G.D., 2019. Transport and loss of ring current electrons inside geosynchronous orbit during the 17 March 2013 storm. J. Geophys. Res. Space Phys. 124. https://doi.org/10.1029/2018JA026031.

Asikainen, T., Mursula, K., 2011. Recalibration of NOAA/MEPED energetic proton measurements. J. Atmos. Solar-Terrestrial Phys. 73, 335–347. https://doi.org/10.1016/j.jastp.2009.12.011.

Asikainen, T., Mursula, K., Maliniemi, V., 2012. Correction of detector noise and recalibration of NOAA/MEPED energetic proton fluxes. J. Geophys. Res. 117, A09204. https://doi.org/10.1029/2012JA017593.

Barth, C.A. et al., 2001. The northern auroral region as observed in nitric oxide. Geophys. Res. Lett. 28, 1463–1466.

Bazilevskaya, G.A., Kalinin, M.S., Krainev, M.B., Makhmutov, V.S., Stozhkov, Y.I., Svirzhevskaya, A.K., et al., 2020. Temporal characteristics of energetic magnetospheric electron precipitation as observed during long-term balloon observations. J. Geophys. Res.: Space Phys. 125. https://doi.org/10.1029/2020JA028033.

Bender, S., Espy, P.J., Paxton, L.J., 2021. Validation of SSUSI-derived auroral electron densities: comparisons to EISCAT data. Ann. Geophys. 39 (5), 899–910. https://doi.org/10.5194/angeo-39-899-2021.

Bender, S. (2023, September). st-bender/pyeppaurora: Version 0.3.0. Zenodo [code]. Zenodo. https://doi.org/10.5281/zenodo.8334549

Blake, J.B. et al., 2013. The Magnetic Electron Ion Spectrometer (MagEIS) Instruments Aboard the Radiation Belt Storm Probes (RBSP) Spacecraft. Space Sci. Rev. 179, 1–4. https://doi.org/10.1007/S11214-013-9991-8.

Blum, L.W., Schiller, Q., Li, X., Millan, R., Halford, A., Woodger, L., 2013. New conjunctive CubeSat and balloon measurements to quantify rapid energetic electron precipitation. Geophys. Res. Lett. 40, 5833–5837. https://doi.org/10.1002/2013GL058546.

Boscher,D., Bourdarie, S., O'Brien, P., Guild, T., Heynderickx, D., Morley, S., Kellerman, A., Roth, C., Evans, H., Brunet, A., Shumko, M., Lemon, C., Claudepierre, S., Nilsson, T., De Donder, E., Friedel, R., Huston, S., Min, K., Drozdov A., IRBEM Contributor Community, 2022. PRBEM/IRBEM: v5.0.0 (IRBEM-5.0.0). Zenodo. https://doi.org/10.5281/zenodo.6867768

Brautigam, D.H., Albert, J.M., 2000. Radial diffusion analysis of outer radiation belt electrons during the October 9, 1990, magnetic storm. J. Geophys. Res. 105 (A1), 291–309. https://doi.org/10.1029/1999JA900344.

Breneman, A.W., Crew, A., Sample, J., Klumpar, D., Johnson, A., Agapitov, O., Kletzing, C.A., 2017. Observations directly linking relativistic electron microbursts to whistler mode chorus: Van Allen Probes and FIREBIRD II. Geophys. Res. Lett. 44, 11265–11272. https://doi.org/10.1002/2017GL075001.

Carpenter, D.L., Anderson, R.R., 1992. An ISEE/whistler model of equatorial electron density in the magnetosphere. J. Geophys. Res. 97 (A2), 1097–1108. https://doi.org/10.1029/91JA01548.

Chaston, C.C., Bonnell, J.W., Kletzing, C.A., Hospodarsky, G.B., Wygant, J.R., Smith, C.W., 2015. Broadband low-frequency electromagnetic waves in the inner magnetosphere. J. Geophys. Res. Space Phys. 120, 8603–8615. https://doi.org/10.1002/2015JA021690.

Chen, L., Artemyev, Z.-J., Zheng, L., Xia, Z., Breneman, A.W., Horne, R. B., 2021. Electron microbursts induced by nonducted chorus waves. Front. Astron. Space Sci. 8. https://doi.org/10.3389/fspas.2021.745927 745927.

Chen, M.W., Lemon, C.L., Hecht, J., Sazykin, S., Wolf, R.A., Boyd, A., Valek, P., 2019. Diffuse auroral electron and ion precipitation effects on RCM-E comparisons with satellite data during the 17 March 2013 storm. J. Geophys. Res. Space Phys. 124, 4194–4216. https://doi.org/10.1029/2019JA026545.

Clilverd, M.A., Rodger, C.J., van deKamp, M., Verronen, P.T., 2020. Electron precipitation from the outer radiation belt during the St. Patrick's day storm 2015: Observations, modeling, and validation. J. Geophys. Res. Space Phys. 125. https://doi.org/10.1029/2019JA027725 e2019JA027725.

Denton, M.H., Thomsen, M.F., Jordanova, V.K., Henderson, M.G., Borovsky, J.E., Denton, J.S., Pitchford, D., Hartley, D.P., 2015. An empirical model of electron and ion fluxes derived from observations at geosynchronous orbit. Space Weather 13, 233–249. https://doi.org/10.1002/2015SW001168.

Drozdov, A.Y., Shprits, Y.Y., Orlova, K.G., Kellerman, A.C., Subbotin, D.A., Baker, D.N., Spence, H.E., Reeves, G.D., 2015. Energetic, relativistic, and ultrarelativistic electrons: Comparison of long-term VERB code simulations with Van Allen Probes measurements. J. Geophys. Res. Space Phys. 120, 3574–3587. https://doi.org/10.1002/2014JA020637.

Drozdov, A.Y., Shprits, Y.Y., Aseev, N.A., Kellerman, A.C., Reeves, G. D., 2017. Dependence of radiation beltsimulations to assumed radial diffusion rates tested for two empirical models of radial transport. Space Weather 15, 150–162. https://doi.org/10.1002/2016SW001426.

Drozdov, A.Y., Usanova, M.E., Hudson, M.K., Allison, H.J., Shprits, Y. Y., 2020. The role of hiss, chorus, and EMIC waves in the modeling of the dynamics of the multi-MeV radiation belt electrons. J. Geophys. Res. Space Phys. 125. https://doi.org/10.1029/2020JA028282.

Drozdov, A.Y., Allison, H.J., Shprits, Y.Y., Elkington, S.R., Aseev, N.A., 2021. A comparison of radial diffusion coefficients in 1-D and 3-D long-term radiation belt simulations. J. Geophys. Res. Space Phys. 126. https://doi.org/10.1029/2020JA028707.

Evans, D.S., Greer, M.S., 2000. Polar orbiting environmental satellite space environment monitor-2: Instrument descriptions and archive data documentation, NOAA Tech. Memo., OAR SEC 93, 93, version 1.4, Boulder, Colo., 2004 Jan

Fang, X., Randall, C.E., Lummerzheim, D., Solomon, S.C., Mills, M.J., Marsh, D.R., Jackman, C.H., Wang, W., Lu, G., 2008. Electron impact ionization: A new parameterization for 100 eV to 1 MeV electrons. J. Geophys. Res. 113, A09311. https://doi.org/10.1029/2008JA013384.

Fang, X., Randall, C.E., Lummerzheim, D., Wang, W., Lu, G., Solomon, S.C., Frahm, R.A., 2010. Parameterization of monoenergetic electron impact ionization. Geophys. Res. Lett. 37, L22106. https://doi.org/10.1029/2010GL045406.

Ferradas, C.P., Jordanova, V.K., Reeves, G.D., Larsen, B.A., 2019. Comparison of electron loss models in the inner magnetosphere during the 2013 St. Patrick's Day geomagnetic storm. J. Geophys. Res. Space Phys. 124 (10), 7872–7888. https://doi.org/10.1029/2019JA026649.

Funke, B., López-Puertas, M., Holt, L., Randall, C.E., Stiller, G.P., von Clarmann, T., 2014. Hemispheric distributions and interannual variability of NOy produced by energetic particle precipitation in 2002–2012. J. Geophys. Res. Atmos. 119, 13565–13582. https://doi.org/10.1002/2014jd022423.

Funke, B., Dudok de Wit, T., Ermolli, I., Haberreiter, M., Kinnison, D., Marsh, D., Nesse, H., Seppälä, A., Sinnhuber, M., Usoskin, I., 2023. Towards the definition of a solar forcing dataset for CMIP7. Geosci. Model Dev. https://doi.org/10.5194/gmd-2023-100.

Funsten, H.O. et al., 2013. Helium, Oxygen, Proton, and Electron (HOPE) Mass Spectrometer for the Radiation Belt Storm Probes Mission. Space Sci. Rev. 179, 1–4. https://doi.org/10.1007/s11214-013-9968-7.

Galand, M., Evans, D.S., 2000. Radiation damage of the proton MEPED detector on POES (TIROS/NOAA) satellites. NOAA Technical Memorandum, Boulder, Colorado OAR 456-SEC. 42.

Glauert, S.A., Horne, R.B., Meredith, N.P., 2014. Three-dimensional electron radiation belt simulations using the BAS Radiation Belt Model with new diffusion models for chorus, plasmaspheric hiss, and lightning-generated whistlers. J. Geophys. Res. Space Phys. 119, 268–289. https://doi.org/10.1002/2013JA019281.

Grishina, A., Shprits, Y., Drozdov, A., Sinnhuber, M., Haenel, F., Wang, D., Szabó-Roberts, M., Wissing, J.M., Bender, S., 2023. Data for: Ring Current Electron Precipitation During the 17 March 2013 Geomagnetic Storm: Underlying Mechanisms and Their Effect on the Atmosphere (Version 1). Zenodo. https://doi.org/10.5281/zenodo.10046626.

Haas, B., Shprits, Y.Y., Allison, H.J., et al., 2023. A missing dusk-side loss process in the terrestrial electron ring current. Sci. Rep. 13, 970. https://doi.org/10.1038/s41598-023-28093-2.

Ionization.de., n.d. Homepage of Ionization. http://www.ionization.de. Accessed October 30, 2023.

Johnson, A.T., Shumko, M., Griffith, B., Klumpar, D.M., Sample, J., Springer, L., Leh, N., Spence, H.E., Smith, S., Crew, A., Handley, M., Mashburn, K.M., Larsen, B.A., Blake, J.B., 2020. The FIREBIRD-II CubeSat mission: Focused investigations of relativistic electron burst intensity, range, and dynamics. Rev. Sci. Instrum. 91 (3). https://doi.org/10.1063/1.5137905 034503.

Kasahara, S., Miyoshi, Y., Yokota, S., Mitani, T., Kasahara, Y., Matsuda, S., et al., 2018. Pulsating aurora from electron scattering by chorus waves. Nature 554 (7692), 338–340. https://doi.org/10.1038/nature25505.

Kennel, C.F., Petschek, H.E., 1966. Limit on stably trapped particle fluxes. J. Geophys. Res. 71 (1), 1–28. https://doi.org/10.1029/JZ071i001p00001.

Knight, H.K., Galkin, I.A., Reinisch, B.W., Zhang, Y., 2018. Auroral Ionospheric E Region Parameters Obtained From Satellite-Based Far Ultraviolet and Ground-Based Ionosonde Observations: Data, Methods, and Comparisons. J. Geophys. Res. Space Phys. 123 (7), 6065–6089. https://doi.org/10.1029/2017ja024822.

Lam, M.M., Horne, R.B., Meredith, N.P., Glauert, S.A., Moffat-Griffin, T., Green, J.C., 2010. Origin of energetic electron precipitation >30 keV into the atmosphere. J. Geophys. Res. 115. https://doi.org/10.1029/2009JA014619 A00F08.

Lauben, D.S., Inan, U.S., Bell, T.F., 2001. Precipitation of radiation belt electrons induced by obliquely propagating lightning-generated whistlers. J. Geophys. Res. 106 (A12), 29,745–29,770.

Li, W., Ni, B., Thorne, R.M., Bortnik, J., Green, J.C., Kletzing, C.A., Kurth, W.S., Hospodarsky, G.B., 2013. Constructing the global distribution of chorus wave intensity using measurements of electrons by the POES satellites and waves by the Van Allen Probes. Geophys. Res. Lett. 40, 4526–4532. https://doi.org/10.1002/grl.50920.

Li, W., Shen, X.-C., Ma, Q., Capannolo, L., Shi, R., Redmon, R.J., et al., 2019. Quantification of energetic Electron precipitation driven by plume whistler mode waves, Plasmaspheric hiss, and exohiss. Geophys. Res. Lett. 46 (7), 3615–3624. https://doi.org/10.1029/2019GL082095.

Lyons, L.R., Thorne, R.M., 1973. Equilibrium structure of radiation belt electrons. J. Geophys. Res. 78 (13), 2142–2149. https://doi.org/10.1029/JA078i013p02142.

Ma, Q., Li, W., Thorne, R.M., Ni, B., Kletzing, C.A., Kurth, W.S., et al., 2015. Modeling inward diffusion and slow decay of energetic electrons in the Earth's outer radiation belt. Geophys. Res. Lett. 42, 987–995. https://doi.org/10.1002/2014GL062977.

Ma, Q., Li, W., Thorne, R.M., Bortnik, J., Kletzing, C.A., Kurth, W.S., Hospodarsky, G.B., 2016. Electron scattering by magnetosonic waves in the inner magnetosphere. J. Geophys. Res. Space Phys. 121, 274–285. https://doi.org/10.1002/2015JA021992.

Ma, Q., Connor, H.K., Zhang, X.-J., Li, W., Shen, X.-C., Gillespie, D., et al., 2020. Global survey of plasma sheet electron precipitation due to whistler mode chorus waves in Earth's magnetosphere. Geophys. Res. Lett. 47. https://doi.org/10.1029/2020GL088798 e2020GL088798.

Ma, Q., Li, W., Zhang, X.-J., Bortnik, J., Shen, X.-C., Connor, H.K., et al., 2021. Global survey of electron precipitation due to hiss waves in the Earth's plasmasphere and plumes. J. Geophys. Res. Space Phys. 126. https://doi.org/10.1029/2021JA029644 e2021JA029644.

Malaspina, D.M., Andersson, L., Ergun, R.E., Wygant, J.R., Bonnell, J. W., Kletzing, C., et al., 2014. Nonlinear electric field structures in the inner magnetosphere. Geophys. Res. Lett. 41, 5693–5701. https://doi.org/10.1002/2014GL061109.

Maliniemi, V., Asikainen, T., Mursula, K., 2014. Spatial distribution of Northern Hemisphere winter temperatures during different phases of the solar cycle. J. Geo-phys. Res. Atmos. 119, 9752–9764. https://doi.org/10.1002/2013JD021343.

Matthes, K., Funke, B., Andersson, M.E., Barnard, L., Beer, J., Charbonneau, P., et al., 2017. Solar forcing for CMIP6 (v3.2). Geosci. Model Dev. 10, 2247–2302. https://doi.org/10.5194/gmd-10-2247-2017.

Maynard, N.C., Chen, A.J., 1975. Isolated cold plasma regions: Observations and their relation to possible production mechanisms. J. Geophys. Res. 80 (7), 1009–1013. https://doi.org/10.1029/JA080i007p01009.

Meredith, N.P., Horne, R.B., Glauert, S.A., Thorne, R.M., Summers, D., Albert, J.M., Anderson, R.R., 2006. Energetic outer zone electron loss timescales during low geomagnetic activity. J. Geophys. Res. 111. https://doi.org/10.1029/2005JA011516 A05212.

Meredith, N.P., Horne, R.B., Glauert, S.A., Anderson, R.R., 2007. Slot region electron loss timescales due to plasmaspheric hiss and lightning-generated whistlers. J. Geophys. Res. 112, A08214. https://doi.org/10.1029/2007JA012413.

Meredith, N.P., Horne, R.B., Thorne, R.M., Anderson, R.R., 2009. Survey of upper band chorus and ECH waves: Implications for the diffuse aurora. J. Geophys. Res. 114, A07218. https://doi.org/10.1029/2009JA014230.

Millan, R.M., Baker, D.N., 2012. Acceleration of Particles to High Energies in Earth's Radiation Belts. Space Sci. Rev. 173, 103–131. https://doi.org/10.1007/s11214-012-9941-x.

Mozer, F.S., Agapitov, O.V., Blake, J.B., Vasko, I.Y., 2018. Simultaneous observations of lower band chorus emissions at the equator and microburst precipitating electrons in the ionosphere. Geophys. Res. Lett. 45, 511–516. https://doi.org/10.1002/2017GL076120.

NASA (n.d.). Solar Proton Events Affecting the Earth Environment. National Aeronautics and Space Administration. https://umbra.nascom.nasa.gov/SEP/. Accessed October 30, 2023.

NASA, n.d. Solar Storm Near Earth Caused by March 15, 2013 Fast CME. NASA Scientific Visualization Studio. https://svs.gsfc.nasa.gov/11225/.

Nesse Tyssøy, H., Sandanger, M.I., Ødegaard, L.-K.-G., Stadsnes, J., Aasnes, A., Zawedde, A.E., 2016. Energetic electron precipitation into the middle atmosphere—constructing the loss cone fluxes from MEPED POES. J. Geophys. Res. Space Phys. 121, 5693–5707. https://doi.org/10.1002/2016JA022752.

Nesse Tyssøy, H., Haderlein, A., Sandanger, M.I., Stadsnes, J., 2019. Intercomparison of the POES/MEPED loss cone electron fluxes with the CMIP6 Parametrization. J. Geophys. Res. Space Phys. 124, 628–642. https://doi.org/10.1029/2018JA025745.

Nesse Tyssøy, H., Sinnhuber, M., Asikainen, T., Bender, S., Clilverd, M. A., Funke, B., Kamp, M., Pettit, J.M., Randall, C.E., Reddmann, T., Rodger, C.J., Rozanov, E., Smith-Johnsen, C., Sukhodolov, T., Verronen, P.T., Wissing, J.M., Yakovchuk, O., 2022. HEPPA III Intercomparison Experiment on Electron Precipitation Impacts: 1. Estimated Ionization Rates During a Geomagnetic Active Period in April 2010. Journal of geophysical research / Space physics 127 (1). https://doi.org/10.1029/2021JA029128.

Ni, B., Thorne, R.M., Meredith, N.P., Shprits, Y.Y., Horne, R.B., 2011a. Diffuse auroral scattering by whistler mode chorus waves: Dependence on wave normal angle distribution. J. Geophys. Res. 116, A10207. https://doi.org/10.1029/2011JA016517.

Ni, B., Thorne, R.M., Shprits, Y.Y., Orlova, K.G., Meredith, N.P., 2011b. Chorus-driven resonant scattering of diffuse auroral electrons in nondipolar magnetic fields. J. Geophys. Res. 116, A06225. https://doi.org/10.1029/2011JA016453.

Ni, B., Bortnik, J., Nishimura, Y., Thorne, R.M., Li, W., Angelopoulos, V., Ebihara, Y., Weatherwax, A.T., 2014. Chorus wave scattering responsible for the Earth's dayside diffuse auroral precipitation: A detailed case study. J. Geophys. Res. Space Phys. 119, 897–908. https://doi.org/10.1002/2013JA019507.

Ødegaard, L.-K.-G., Tyssøy, H.N., Søraas, F., Stadsnes, J., Sandanger, M.I., 2017. Energetic electron precipitation in weak to moderate corotating interaction region-driven storms. J. Geophys. Res. Space Phys. 122, 2900–2921. https://doi.org/10.1002/2016JA023096.

Orlova, K., Shprits, Y., 2014. Model of lifetimes of the outer radiation belt electrons in a realistic magnetic field using realistic chorus wave parameters. J. Geophys. Res. Space Phys. 119, 770–780. https://doi.org/10.1002/2013JA019596.

Orlova, K., Spasojevic, M., Shprits, Y., 2014. Activity-dependent global model of electron loss inside the plasmasphere. Geophys. Res. Lett. 41, 3744–3751. https://doi.org/10.1002/2014GL060100.

Orlova, K., Shprits, Y., Spasojevic, M., 2016. New global loss model of energetic and relativistic electrons based on Van Allen Probes measurements. J. Geophys. Res. Space Phys. 121, 1308–1314. https://doi.org/10.1002/2015JA021878.

Paxton, L.J., Meng, C.-I., Fountain, G.H., Ogorzalek, B.S., Darlington, E.H., Gary, S.A., Smith, B.E., 1992. Special sensor ultraviolet spectrographic imager: an instrument description. In: Chakrabarti, S., Christensen, A.B. (Eds.), Instrumentation for Planetary and Terrestrial Atmospheric Remote Sensing. SPIE.

Paxton, L.J., Schaefer, R.K., Zhang, Y., Kil, H., 2017. Far ultraviolet instrument technology. J. Geophys. Res. Space Phys. 122 (2), 2706–2733. https://doi.org/10.1002/2016ja023578.

Paxton, L.J., Schaefer, R.K., Zhang, Y., Kil, H., Hicks, J.E., 2018. SSUSI and SSUSI-Lite: providing space situational awareness and support for over 25 years. Johns Hopkins APL Tech. Dig. 34, 388–400.

Picone, J.M., Hedin, A.E., Drob, D.P., Aikin, A.C., 2002. NRLMSISE-00 empirical model of the atmosphere: statistical comparisons and scientific issues. J. Geophys. Res. 107 (A12), 1468. https://doi.org/10.1029/2002JA009430.

Randall, C.E., Harvey, V.L., Manney, G.L., Orsolini, Y., Codrescu, M., Sioris, C., et al., 2005. Stratospheric effects of energetic particle precipitation in 2003–2004. Geophys. Res. Lett. 32 (5), L05802. https://doi.org/10.1029/2004gl022003.

Randall, C.E., Harvey, V.L., Singleton, C.S., Bailey, S.M., Bernath, P.F., Codrescu, M., Nakajima, H., Russell III, J.M., 2007. Energetic particle precipitation effects on the Southern Hemisphere stratosphere in 1992–2005. J. Geophys. Res. 112, D08308. https://doi.org/10.1029/2006JD007696.

Reidy, J.A., Horne, R.B., Glauert, S.A., Clilverd, M.A., Meredith, N.P., Woodfield, E.E., et al., 2021. Comparing electron precipitation fluxes calculated from pitch angle diffusion coefficients to LEO satellite observations. J. Geophys. Res. Space Phys. 126. https://doi.org/10.1029/2020JA028410 e2020JA028410.

Richmond, A.D., 1995. Ionospheric electrodynamics using magnetic apex coordinates. J. Geomagnet. Geoelectr. 47 (2), 191–212. https://doi.org/10.5636/jgg.47.191.

Rodger, C.J., Carson, B.R., Cummer, S.A., Gamble, R.J., Clilverd, M.A., Green, J.C., et al., 2010a. Contrasting the efficiency of radiation belt losses caused by ducted and nonducted whistler-mode waves from ground-based transmitters. J. Geophys. Res. 115, A12208. https://doi.org/10.1029/2010JA015880.

Rodger, C.J., Clilverd, M.A., Green, J.C., Lam, M.M., 2010b. Use of POES SEM-2 observations to examine radiation belt dynamics and energetic electron precipitation into the atmosphere. J. Geophys. Res. 115, A04202. https://doi.org/10.1029/2008JA014023.

Rodriguez, J.V., Krosschell, J.C., Green, J.C., 2014. Intercalibration of goes 8–15 solar proton detectors. Space Weather 12, 92–109. https://doi.org/10.1002/2013sw000996.

Roederer, J.G., 1970. Dynamics of Geomagnetically Trapped Radiation. Springer, Berlin Heidelberg https://doi.org/10.1007/978-3-642-49300-3.

Rozanov, E., Calisto, M., Egorova, T., et al., 2012. Influence of the precipitating energetic particles on atmospheric chemistry and climate. Surv. Geophys. 33, 483–501. https://doi.org/10.1007/s10712-012-9192-0.

Rozanov, E.V., Callis, L.B., Schlesinger, M., Yang, F., Andronova, N., Zubov, V.A., 2005. Atmospheric response to NOy source due toenergetic electron precipitation. Geophys. Res. Lett. 32, L14811. https://doi.org/10.1029/2005gl023041.

Sanchez, E.R., Ma, Q., Xu, W., Marshall, R.A., Bortnik, J., Reyes, P., et al., 2022. A test of energetic particle precipitation models using simultaneous incoherent scatter radar and Van Allen Probes observations. J. Geophys. Res. Space Phys. 127. https://doi.org/10.1029/2021JA030179.

Sandanger, M. I., L.-K. G. Ødegaard, H. Nesse Tyssøy, J. Stadsnes, F. Søraas, K. Oksavik, and K. Aarsnes (2015), In-flight calibration of NOAA POES proton detectors—Derivation of the MEPED correction factors, J. Geophys. Res. Space Physics,120, 9578–9593, doi: https://doi.org/10.1002/2015JA021388.

Schmidt, H., Brasseur, G.P., Charron, M., Manzini, E., Giorgetta, M.A., Diehl, T., Fomichev, V.I., Kinnison, D., Marsh, D., Walters, S., 2006. The HAMMONIA chemistry climate model: sensitivity of the mesopause region to the 11-year solar cycle and CO2 doubling. J. Clim. 19 (16), 3903–3931. https://doi.org/10.1175/JCLI3829.1.

Schröter, J., Heber, B., Steinhilber, F., Kallenrode, M.B., 2006. Energetic particles in the atmosphere: a Monte-Carlo simulation. Adv. Space Res. 37 (8), 1597–1601. https://doi.org/10.1016/j.asr.2005.05.085.

Schulz, M., Lanzerotti, L.J., 1974. Particle Diffusion in the Radiation Belts, Vol. 7. Springer Science & Business Media.

Selesnick, R.S., Blake, J.B., 2000. On the source location of radiation belt relativistic electrons. J. Geophys. Res. 105 (A2), 2607–2624. https://doi.org/10.1029/1999JA900445.

Seppälä, A., Randall, C.E., Clilverd, M.A., Rozanov, E., Rodger, C.J., 2009. Geomagnetic activity and polar surface air temperature variability. J. Geophys. Res. 114, A10312. https://doi.org/10.1029/2008JA014029.

Shen, Y., Artemyev, A.V., Zhang, X.-J., Angelopoulos, V., Vasko, I.Y., Turner, D.L., Tsai, E., Wilkins, C., Ergun, R.E., Giles, B.L., Russell, C. T., 2022. Tens to hundreds of keV electron precipitation driven by kinetic Alfvén waves during an electron injection. J. Geophys. Res. Space Phys. 127. https://doi.org/10.1029/2022JA030360 e2022JA030360.

Shprits, Y., Elkington, N., Meredith, N., Subbotin, D., 2008b. Review of modeling of losses and sources of relativistic electrons in the outer radiation belts: I. Radial transport. J. Atmos. Sol. Terr. Phys. 70 (14), 1679–1693. https://doi.org/10.1016/j.jastp.2008.06.014.

Shprits, Y.Y., Ni, B., 2009. Dependence of the quasi-linear scattering rates on the wave normal distribution of chorus waves. J. Geophys. Res. 114, A11205. https://doi.org/10.1029/2009JA014223.

Shprits, Y., Subbotin, D., Meredith, N., Elkington, S., 2008a. Review of modeling of losses and sources of relativistic electrons in the outer

radiation belts: II. Local acceleration and loss. J. Atmos. Sol. Terr. Phys. 70 (14), 1694–1713. https://doi.org/10.1016/j.jastp.2008.06.014.

Shprits, Y.Y., Thorne, R.M., Horne, R.B., Summers, D., 2006a. Bounce-averaged diffusion coefficients for field-aligned chorus waves. J. Geophys. Res. 111, A10225. https://doi.org/10.1029/2006JA011725.

Shprits, Y.Y., Thorne, R.M., Friedel, R., Reeves, G.D., Fennell, J., Baker, D.N., Kanekal, S.G., 2006b. Outward radial diffusion driven by losses at magnetopause. J. Geophys. Res. 111, A11214. https://doi.org/10.1029/2006JA011657.

Shprits, Y.Y., Kellerman, A.C., Drozdov, A.Y., Spence, H.E., Reeves, G. D., Baker, D.N., 2015. Combined convective and diffusive simulations: VERB-4D comparison with 17 March 2013 Van Allen Probes observations. Geophys. Res. Lett. 42, 9600–9608. https://doi.org/10.1002/2015GL065230.

Shprits, Y.Y., Allison, H.J., Wang, D., Drozdov, A., Szabo-Roberts, M., Zhelavskaya, I., Vasile, R., 2022. A new population of ultra-relativistic electrons in the outer radiation zone. J. Geophys. Res. Space Phys. 127. https://doi.org/10.1029/2021JA030214 e2021JA030214.

Shprits, Y.Y., Michaelis, I., Wang, D., Allison, H., Vasile, R., Runov, A., et al., 2023. MLT dependence of relativistic electron scattering into the drift loss cone: Measurements from ELFIN-L on board Lomonosov spacecraft. Geophys. Res. Lett. 50. https://doi.org/10.1029/2023GL103342 e2023GL103342.

Shprits, Y., Subbotin, D., Drozdov, A., et al., 2013. Unusual stable trapping of the ultrarelativistic electrons in the Van Allen radiation belts. Nature Phys. 9, 699–703. https://doi.org/10.1038/nphys2760.

Shprits, Y.Y., Thorne, R.M., 2004. Time dependent radial diffusion modeling of relativistic electrons with realistic loss rates. Geophys. Res. Lett. 31, L08805. https://doi.org/10.1029/2004GL019591.

Sillanpää, I., Ganushkina, N.Y., Dubyagin, S., Rodriguez, J.V., 2017. Electron fluxes at geostationary orbit from GOES MAGED data. Space Weather 15, 1602–1614. https://doi.org/10.1002/2017SW001698.

Sinnhuber, M., Funke, B., 2020. Energetic Electron Precipitation into the Atmosphere. Elsevier, pp. 279–321 https://doi.org/10.1016/B978-0-12-813371-2.00009-3.

Sinnhuber, M., Nieder, H., Wieters, N., 2012. Energetic particle precipitation and the chemistry of the mesosphere/lower thermosphere. Surv. Geophys. 33, 1281–1334. https://doi.org/10.1007/s10712-012-9201-3.

Sinnhuber, M., Berger, U., Funke, B., Nieder, H., Reddmann, T., Stiller, G., et al., 2018. NO y production, ozone loss and changes in net radiative heating due to energetic particle precipitation in 2002–2010. Atmos. Chem. Phys. 18, 1115–1147. https://doi.org/10.5194/acp-18-1115-2018.

Sinnhuber, M., Nesse Tyssøy, H., Asikainen, T., Bender, S., Funke, B., Hendrickx, K., Pettit, J.M., Reddmann, T., Rozanov, E., Schmidt, H., Smith-Johnsen, C., Sukhodolov, T., Szeląg, M.E., Kamp, M., Verronen, P.T., Wissing, J.M., Yakovchuk, O.S., 2021. Heppa III intercomparison experiment on electron precipitation impacts: 2. model-measurement intercomparison of nitric oxide (NO) during a geomagnetic storm in April 2010. J. Geophys. Res./Space Phys. 127 (1). https://doi.org/10.1029/2021JA029466 e2021JA029466.

Sinnhuber, B.-M., Stiller, G., Ruhnke, R., von Clarmann, T., Kellmann, S., Aschmann, J., 2011. Arctic winter 2010/2011 at the brink of an ozone hole. Geophys. Res. Lett. 38, L24814. https://doi.org/10.1029/2011GL049784.

Siskind, D.E., Nedoluha, G.E., Russell, J.M., Randall, C.E., Fromm, M., 2000. An assessment of Southern Hemisphere stratospheric NOx enhancements due to transport from the upper atmosphere. Geophys. Res. Lett. 27, 329–332.

Solomon, S., Crutzen, P.J., Roble, R.G., 1982. Photochemical coupling between the thermosphere and the lower atmosphere: 1. Odd nitrogen from 50 to 120 km. J. Geophys. Res. 87 (C9), 7206–7220. https://doi.org/10.1029/JC087iC09p07206.

Spence, H.E., Reeves, G.D., Baker, D.N., et al., 2013. Science Goals and Overview of the Radiation Belt Storm Probes (RBSP) Energetic Particle, Composition, and Thermal Plasma (ECT) Suite on NASA's Van Allen Probes Mission. Space Sci. Rev. 179, 311–336. https://doi.org/10.1007/s11214-013-0007-5.

Stern, D.P., 1975. The motion of a proton in the equatorial magnetosphere. J. Geophys. Res. 80 (4), 595–599. https://doi.org/10.1029/JA080i004p00595.

Subbotin, D.A., Shprits, Y.Y., Ni, B., 2011. Long-term radiation belt simulation with the VERB 3-D code: comparison with CRRES observations. J. Geophys. Res. 116, A12210. https://doi.org/10.1029/2011JA017019.

Subbotin, D.A., Shprits, Y.Y., 2012. Three-dimensional radiation belt simulations in terms of adiabatic invariants using a single numerical grid. J. Geophys. Res. 117, A05205. https://doi.org/10.1029/2011JA017467.

Summers, D., Ni, B., Meredith, N.P., Horne, R.B., Thorne, R.M., Moldwin, M.B., Anderson, R.R., 2008. Electron scattering by whistler-mode ELF hiss in plasmaspheric plumes. J. Geophys. Res. 113, A04219. https://doi.org/10.1029/2007JA012678.

Teng, S., Han, D.-S., Liang, J., Zhang, Q., Sun, J., Wang, S., et al., 2023. Conjugate observation of whistler mode chorus, ECH waves and dayside diffuse aurora by MMS and ground-based Yellow River Station. J. Geophys. Res. Space Phys. 128. https://doi.org/10.1029/2023JA031865.

Thébault, E., Finlay, C.C., Beggan, C.D., et al., 2015. International Geomagnetic Reference Field: the 12th generation. Earth Planet Sp 67, 79. https://doi.org/10.1186/s40623-015-0228-9.

Thorne, R., 1977. Energetic radiation belt electron precipitation: a natural depletion mechanism for stratospheric ozone. Science 195 (4275), 287–289. https://doi.org/10.1126/science.195.4275.287.

Thorne, R.M., 2010. Radiation belt dynamics: The importance of wave-particle interactions. Geophys. Res. Lett. 37, L22107. https://doi.org/10.1029/2010GL044990.

Thorne, R.M., O'Brien, T.P., Shprits, Y.Y., Summers, D., Horne, R.B., 2005. Timescale for MeV electron microburst loss during geomagnetic storms. J. Geophys. Res. 110, A09202. https://doi.org/10.1029/2004JA010882.

Tsyganenko, N.A., 1989. A magnetospheric magnetic field model with a warped tail current sheet. Planet. Space Sci. 37, 5–20. https://doi.org/10.1016/0032-0633(89)90066-4.

Tsyganenko, N.A., Singer, H.J., Kasper, J.C., 2003. Storm-time distortion of the inner magnetosphere: How severe can it get? J. Geophys. Res. 108 (A5), 1209. https://doi.org/10.1029/2002JA009808.

Tsyganenko, N.A., Sitnov, M.I., 2005. Modeling the dynamics of the inner magnetosphere during strong geomagnetic storms. J. Geophys. Res. 110, A03208. https://doi.org/10.1029/2004JA010798.

Tu, W., Selesnick, R., Li, X., Looper, M., 2010. Quantification of the precipitation loss of radiation belt electrons observed by SAMPEX. J. Geophys. Res. 115, A07210. https://doi.org/10.1029/2009JA014949.

Turunen, E., Verronen, P.T., Seppälä, A., Rodger, C.J., Clilverd, M.A., Tamminen, J., Enell, C.-F., Ulich, T., 2009. Impact of different energies of precipitating particles on NOx generation in the middle and upper atmosphere during geomagnetic storms. J. Atmospher. Solar-Terrest. Phys. 71 (10–11), 1176–1189. https://doi.org/10.1016/j.jastp.2008.07.005.

van de Kamp, M., Seppälä, A., Clilverd, M.A., Rodger, C.J., Verronen, P. T., Whittaker, I.C., 2016. A model providing long-term data sets of energetic electron precipitation during geomagnetic storms. J. Geophys. Res. Atmos. 121, 12520–12540. https://doi.org/10.1002/2015JD024212.

Volland, H., 1973. A semiempirical model of large-scale magnetospheric electric fields. J. Geophys. Res. 78 (1), 171–180. https://doi.org/10.1029/JA078i001p00171.

Wang, C. et al., 2017. Modeling radiation belt dynamics using a 3-D layer method code. J. Geophys. Res. Space Phys. 122, 8642–8658. https://doi.org/10.1002/2017JA024143.

Wang, D., Shprits, Y.Y., 2019. On how high-latitude chorus waves tip the balance between acceleration and loss of relativistic electrons. Geophys. Res. Lett. 46, 7945–7954. https://doi.org/10.1029/2019GL082681.

Wang, D., Shprits, Y.Y., Zhelavskaya, I.S., Agapitov, O.V., Drozdov, A. Y., Aseev, N.A., 2019. Analytical chorus wave model derived from

Van Allen Probe observations. J. Geophys. Res. Space Phys. 124, 1063–1084. https://doi.org/10.1029/2018JA026183.

Wang, D., Shprits, Y.Y., Zhelavskaya, I.S., Effenberger, F., Castillo, A., Drozdov, A.Y., et al., 2020. The effect of plasma boundaries on the dynamic evolution of relativistic radiation belt electrons. J. Geophys. Res. Space Phys. 125. https://doi.org/10.1029/2019JA027422.

Weimer, D.R., 2005. Improved ionospheric electrodynamic models and application to calculating Joule heating rates. J. Geophys. Res. 110, A05306. https://doi.org/10.1029/2004JA010884.

Wissing, J.M., Kallenrode, M.-B., 2009. Atmospheric Ionization Module Osnabrück (AIMOS): A 3-D model to determine atmospheric ionization by energetic charged particles from different populations. J. Geophys. Res. 114, A06104. https://doi.org/10.1029/2008JA013884.

WMO. (2018). Scientific assessment of ozone depletion: 2018. World Meteorological Organization Report. Retrieved from https://csl.noaa.gov/assessments/ozone/2018

Yakovchuk, O., Wissing, J.M., 2019. Magnetic local time asymmetries in precipitating electron and proton populations with and without substorm activity. Ann. Geophys. 37, 1063–1077. https://doi.org/10.5194/angeo-37-1063-2019.

Yando, K., Millan, R.M., Green, J.C., Evans, D.S., 2011. A Monte Carlo simulation of the NOAA POES Medium Energy Proton and Electron Detector instrument. J. Geophys. Res. 116, A10231. https://doi.org/10.1029/2011JA016671.

Yu, Y., Jordanova, V.K., Ridley, A.J., Albert, J.M., Horne, R.B., Jeffery, C.A., 2016. A new ionospheric electron precipitation module coupled with RAM-SCB within the geospace general circulation model. J. Geophys. Res. Space Phys. 121, 8554–8575. https://doi.org/10.1002/2016JA022585.

Yu, Y., Hosokawa, K., Ni, B., Jordanova, V.K., Miyoshi, Y., Cao, J., et al., 2022. On the importance of using event-specific wave diffusion rates in modeling diffuse electron precipitation. J. Geophys. Res. Space Phys. 127. https://doi.org/10.1029/2021JA029918 e2021JA029918.

Yu, X., Yuan, Z., Yu, J., et al., 2023. Diffuse auroral precipitation driven by lower-band chorus second harmonics. Nat. Commun. 14, 438. https://doi.org/10.1038/s41467-023-36095-x.

Zhang, X.-J., Angelopoulos, V., Ni, B., Thorne, R.M., 2015. Predominance of ECH wave contribution to diffuse aurora in Earth's outer magnetosphere. J. Geophys. Res. Space Phys. 120, 295–309. https://doi.org/10.1002/2014JA020455.